

Accepted Manuscript

HST/STIS Observations and Simulation of Io's Emission Spectrum in Jupiter Shadow: Probing Io's Jupiter-facing Eclipse Atmosphere

L.M. Trafton, C.H. Moore, D.G. Goldstein, P.L. Varghese, M.A. McGrath

PII: S0019-1035(12)00254-0

DOI: <http://dx.doi.org/10.1016/j.icarus.2012.06.025>

Reference: YICAR 10269

To appear in: *Icarus*

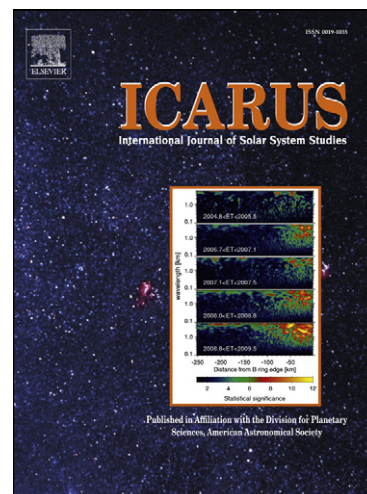
Received Date: 10 January 2012

Revised Date: 11 June 2012

Accepted Date: 11 June 2012

Please cite this article as: Trafton, L.M., Moore, C.H., Goldstein, D.G., Varghese, P.L., McGrath, M.A., HST/STIS Observations and Simulation of Io's Emission Spectrum in Jupiter Shadow: Probing Io's Jupiter-facing Eclipse Atmosphere, *Icarus* (2012), doi: <http://dx.doi.org/10.1016/j.icarus.2012.06.025>

This is a PDF file of an unedited manuscript that has been accepted for publication. As a service to our customers we are providing this early version of the manuscript. The manuscript will undergo copyediting, typesetting, and review of the resulting proof before it is published in its final form. Please note that during the production process errors may be discovered which could affect the content, and all legal disclaimers that apply to the journal pertain.



HST/STIS Observations and Simulation of Io's Emission Spectrum in Jupiter Shadow: Probing Io's Jupiter-facing Eclipse Atmosphere¹

L. M. Trafton^{ab}, C. H. Moore^{cd},
D. G. Goldstein^e, P. L. Varghese^f, and M. A. McGrath^g

^aThe University of Texas, Department of Astronomy,
1 University Station, C1400, Austin, TX 78712-0259

^bCorresponding Author 512 471-1476; E-mail address: lmt@astro.as.utexas.edu

^cThe University of Texas, Department of Aerospace Mechanics,
1 University Station, C1400, Austin, TX 78712-0259

^dNow at Nanoscale and Reactive Processes, Sandia National Laboratories,
MS 1322, PO Box 5800, Albuquerque, NM 87185-1322

^eThe University of Texas, Department of Aerospace Mechanics,
1 University Station, C1400, Austin, TX 78712-0259

^fThe University of Texas, Department of Aerospace Mechanics,
1 University Station, C1400, Austin, TX 78712-0259

^gNASA's MSFC, 112 Lake Pointe Circle, Huntsville, AL, 35824

Pages: 61 with Figures and Tables

Tables: 3

Figures: 17

¹Based on observations made with the NASA/ESA Hubble Space Telescope, obtained from the Data Archive at the Space Telescope Science Institute, which is operated by the Association of Universities for Research in Astronomy, Inc., under NASA contract NAS 5-26555. These observations are associated with programs #HST-GO-08169.09-A and HST-AR-10322.01-A.

Abstract

We report the detection of SO₂ emission from Io in Jupiter's shadow, peaking near 26 Rayleigh/Å around 3150 Å, and emission from its associated excitation-dissociation products, SO in the 2550 Å band and S I in the 1800 and 1900 Å multiplets. In addition, an unidentified emission spectrum was discovered between ~4100 Å and ~5700 Å, which appears to be a vibronic band. Its spectral lines are listed in neither the GEISA nor HITRAN database. The line spacing and wavelength regime are characteristic of molecular bending modes, which would imply a molecule with three or more atoms; e.g., SO₂ or S₂O. Alternative candidates for this species are positive or negative ions of SO₂ and its daughter species. The wavelength-averaged intensity of this unidentified species is bracketed by intensities imaged through Galileo and Cassini filters when Io was in eclipse. Both the unidentified and SO₂ emission are brighter on Io's NE half (in the Jovian system), which is the side closer to Jupiter, but the unidentified emission is more asymmetric, suggesting a connection with Io's wake emission or with volcanic activity. Weakening of the emission intensity between the early eclipse-resolved spectra indicate partial atmospheric collapse due to freezeout of the atmospheric column and the decay of energetic photoelectrons. Specific plume activity is not well constrained through examination of the disk-averaged mid-ultraviolet (MUV) emission spectrum. Simulating the observations using laboratory data published for the electron impact cross sections of SO₂ indicates that this emission is consistent with dissociative excitation of SO₂ by thermal electrons in the Jovian plasma torus plus a minor non-thermal electron component. Owing to uncertainty in the density and mean energy of non-thermal electrons, the observations are insufficiently constrained to extract the temperature of the upstream electrons. Without any non-thermal electrons, the best fit upstream electron temperature is ~10 eV; however, prior observations found the Jovian torus thermal electron temperature near Io to be 4-6 eV and thus a non-thermal component is required to reduce the best-fit simulated electron temperature. The upstream temperature of electrons mixed with a non-thermal component that produced agreement between the simulated and observed absolute peak intensities (at 2550 Å and 3150 Å) and their ratio, is $T_e=5-6$ eV with an accompanying non-thermal component of electrons that is 5% of the thermal density and has a mean electron energy of 35 eV.

1 Introduction

Being the primary source of charged particles in the Jovian magnetosphere, Io plays a central role in dictating magnetospheric processes and phenomena. The primary process by which Io populates the magnetosphere is uncertain but must depend on the complex structure and composition of Io's atmosphere and its interaction with the Jovian plasma torus. Definitive knowledge of excitation scenarios and pathways has been lacking. For this reason, a coordinated, HST-Galileo campaign was undertaken to jointly study Io (Bagenal et al. 1999). The HST/STIS observations reported here were part of this campaign. Their purpose was to study the atomic and molecular emission spectrum of Io's atmosphere when in Jupiter's shadow; i.e., when excited solely by charged-particle impact, without the added complication of excitation by solar EUV radiation. Io's tidal interaction with Jupiter and Europa is sufficient to melt part of its crust, causing volcanoes, which support a thin volatile, spatially variable atmosphere and surface frost. This atmosphere consists of localized plumes from active volcanoes and lava lakes, and gas sublimed from widespread volatile frost, which is primarily SO₂ originally deposited locally by volcanoes. Io's dayside atmosphere is patchy and constrained to low- to mid-latitudes due to the distribution of frosts and plumes. The frost-supported component, which we term the "sublimation atmosphere", is widespread but patchy owing to the distribution of frosts and plumes. This sublimation component constitutes the bulk of the daytime atmosphere but much of it apparently freezes out at night and during eclipse (Geissler et al. 1999; 2004).

A number of reviews are available that summarize Io's atmosphere and surface; e.g., Spencer and Schneider (1996); McEwen et al. (1998a,b); Lellouch (1996; 2005); Lopes-Gautier (2000); McGrath et al. (2004); and Lopes and Spencer (2007). Besides SO₂ and small amounts of Na, K and Cl, the species SO, S, S₂, and O have been observed in Io's atmosphere. Dissociative excitation of SO₂ by plasma torus electrons and photo-dissociation produces some of these species. The photo-dissociated products persist well into eclipse. Zotolov and Fegley (2000) have computed the equilibrium

mole fractions vs. vent temperature and S/O ratio, but the extent to which volcanoes actually contribute these gases is unknown. Spacecraft and HST observations have measured Io's SO₂ column abundance, initially for hemispherical averages, then later with the disk resolved. Disk-averaged observations taken in 1993 revealed Io's leading hemisphere to have less SO₂ gas than its trailing hemisphere (Trafton et al. 1996). The Jupiter-facing hemisphere, which is the one observable from Earth during eclipse, has a lower SO₂ column than the anti-Jupiter hemisphere (Jessup et al. 2004; Spencer et al. 2005; Feaga et al. 2009; Tsang et al. 2012).

The most detailed mapping of Io's SO₂ column is based on an analysis of HST/STIS observations of the atmospheric absorption of solar Ly- α diffusely reflected by Io's disk (Feaga et al. 2009). These observations indicate that the local SO₂ vertical column abundance varies with latitude and longitude ranging from $\sim 10^{13}$ (at the poles) to $6 \times 10^{16} \text{ cm}^{-2}$ (in the high density anti-jovian equatorial regions, away from plumes). Thus, these observations confirm that SO₂ gas is concentrated at lower latitudes and on the anti-Jupiter side of Io. Higher vertical column abundances in the literature historically reflect observations that resolve Prometheus-type plumes. That is vertical column densities $\sim 10^{17} \text{ cm}^{-2}$ or greater have been inferred from the Prometheus-type plumes (Jessup et al. 2004, Jessup and Spencer, 2012); while for the Pele-type plumes vertical column densities $\sim 4 \pm 3 \times 10^{16} \text{ cm}^{-2}$ have been consistently found (McGrath et al. 2000, Spencer et al. 2000, Jessup and Spencer, 2012). Thus, the tangential column abundance inferred for large Pele plume based on HST detections of the plumes along Io's limb via absorption of Jovian light correspond to $\sim 8 \pm 6 \times 10^{16} \text{ cm}^{-2}$ (Jessup and Spencer, 2012). Simulations of the 1979 Voyager imaged Pele plume eruption predict a non-uniform gas distribution with tangential column densities ranging from $4.5 \times 10^{17} \text{ cm}^{-2}$ at the vent, to $2 \times 10^{17} \text{ cm}^{-2}$ in the upper canopy; to $9 \times 10^{16} \text{ cm}^{-2}$ for the bulk of the plume area located between the vent and the plume canopy (Zhang et al. 2004).

Electron impact excitation appears to be the primary process for exciting Io's aurorae in Jupiter's shadow, resulting in emission from the dissociative excitation products

of SO₂; namely, SO, S I, S II, O I, and O II. Owing to nightly cooling of Io in its tidally locked orbit about Jupiter, the temperature of the surface frost drops significantly so that the sublimation atmosphere may undergo extreme variation in column abundance unless a non-condensable gas is present (Moore et al. 2009). The same is expected for Io's daytime atmosphere during its daily 2-hr solar eclipse by Jupiter. Clarke et al. (1994) observed that Io's FUV emission from multiplets of sulfur and oxygen decreased by roughly a factor of 3 within 20 min of eclipse ingress. Part of this was due to the cutoff of EUV solar excitation. They concluded that the decrease is consistent with plasma torus impact excitation with a decrease in the atmospheric column. However, they did not have the sensitivity to detect SO₂ and SO emission in eclipse.

The relative contribution of volcanic plumes and the sublimation atmosphere to Io's atmosphere varies diurnally and seasonally (e.g., Tsang et al. 2012), but is not well known (Saur & Strobel 2004). From FUV spectra of New Horizons and HST taken during Io eclipse, Retherford et al. (2007) report that the contribution of the volcanoes to Io's dayside atmosphere is 1–3%. During eclipse, the volcanic component of Io's atmosphere may be significant since aurorae are observed to remain bright throughout eclipse (Geissler et al. 2004; and Retherford et al. also found disk averaged intensities which decreased by a factor of 2 during the initial 40–60 min after ingress and then changed little over the rest of the eclipse). Aurorae linked to volcanoes have even been observed to brighten during eclipse, which could occur if a reduced sublimation atmosphere permits greater plasma penetration into the plumes (Geissler et al., 1999). However, a large non-condensed gas fraction during eclipse might inhibit the freezeout of enough SO₂ to explain the eclipse emission (Moore et al. 2009).

It was recognized by Geissler et al. (2004) on the basis of narrow-band Cassini ISS images of Io in eclipse, that there must be an additional source of emission in Io's visual spectrum because the SO₂ electron impact spectrum, which peaks near 3150 Å, falls off too rapidly to explain the green emission observed in those images. They suggested that this source is S₂, which has been detected in Pele type plumes (Spencer et al.

2000). However, this suggestion could not be tested because laboratory spectra of S_2 in this wavelength range have been lacking. Moreover, published spectral observations of Io in eclipse have also been lacking to help resolve this issue. We show in this paper that there is indeed an unidentified molecular spectrum spanning this region that can help to constrain the species identity.

Simulation of emission phenomena is the basis for understanding processes that control and shape Io's atmosphere and its interaction with the plasma environment. Aurorae serve as a unique diagnostic probe of Io's atmospheric structure and composition, and they also may constrain the temperature and incident flux of the Jovian plasma torus electrons. However, Io's diagnostic mid-ultraviolet (MUV) to visible aurorae are too faint to be seen against the bright, dayside disk. They are visible only on Io's night side or when Io is in Jupiter's shadow. A compensating advantage is that their analysis is simplified by the absence of solar EUV excitation. From Earth, Io's aurorae can only be observed during eclipse (and away from Jupiter opposition); e.g., Retherford et al. (2000; 2003).

The best maps of the frost distribution were obtained from the Galileo NIMS observations of Io (Doute et al. 2001). They include the geographical distribution and physical characterization of the frosts, which assumes they are optically thick and are geographically mixed with other sulfur-bearing compounds. The frost is more prevalent on the anti-Jupiter side of Io and appears adequate to support an atmosphere that falls off smoothly with increasing latitude due to the reduced insolation (Jessup et al. 2004). These deposits may be suitable tracers of various phenomena, including volcanic production and emission, atmospheric transportation, condensation, metamorphism, irradiation, and sublimation, that occur throughout the SO_2 cycle (Walker et al. 2010; Gratiy et al. 2010).

In the present work, we present spectra of Io taken in eclipse from 1750Å to 5700Å obtained by HST/STIS and seek to constrain the interaction of Io's Jupiter-facing atmosphere with the Jovian plasma torus through 3-D Monte Carlo electron transport

simulations of Io’s MUV-visible spectra. In Section 2 we present the observations; Section 3 describes our data reduction strategy and interpretation; analysis via simulated spectra is presented in Section 4; and Sections 5 and 6 present the discussion and conclusions.

2 Observations

The observations were obtained using HST/STIS following the pre-opposition quadrature of Jupiter that occurred on July 26, 1999 and are summarized in Table 1 and Table 2. The sky background consisted of the diffusely reflected Jovian light that was scattered into the STIS spectrograph aperture. Its spectrum consisted of the Jovian spectrum modified by convolution over a range of Doppler shifts arising from Jupiter’s rotation. The observations were designed to minimize this background. In particular, the STIS nominal 2” x 2” aperture, having dimensions 2.”035 spatial x 2.”012 spectral (STScI communication), was selected to prevent any Jovian light from directly entering the spectrograph. Jupiter’s $\sim 11.4^\circ$ solar phase angle on the dates of observation allowed enough offset of Io’s line of sight, which was west of Jupiter, to observe its eclipse without excessive Jovian background. On Aug 7 and Aug 18 of that year, Io’s diameter was 1.”08 and 1.”12, respectively.

Io was acquired and tracked using the JPL NAIF DE-406 ephemeris. Acquisition images showed that Io was close to being centered in the STIS aperture on both dates. The time of umbral ingress was determined from this ephemeris. Two consecutive exposures were taken after umbra entry on each date. The 7 Aug 1999 observations were made using the CCD detector with grating G430L to obtain Io’s “NUV-visible” spectrum between 2900 Å and 5700 Å. The 18 Aug 1999 observations employed the MAMA detector with grating G230L to obtain Io’s “UV” spectrum between 1750 Å and 3200 Å, slightly overlapping the CCD spectrum to facilitate merging. The CCD pixel size was 0.”051 square with an average dispersion of 2.75 Å/pixel. For the MAMA observations, the pixel size was 0.”0245 x 0.”0248 (spectral x spatial)

Table 1: HST/STIS Observations of Io in Jupiter Shadow

Date	Obs start ^a	Exp	Time into ^b	Orbital	Sub-Io ^c	Io magnetic ^d
(UT)	(UT)	(sec)	total eclipse (min)	longitude (deg)	CML (deg)	latitude (deg)
CCD/G430L						
1999 Aug 7	16:14:06	720	13-25	343	236	+8.8
1999 Aug 7	16:28:18	694	27-39	345	240	+8.1
MAMA/G230L						
1999 Aug 18	6:54:26	800	1-14	342	114	-0.2
1999 Aug 18	7:10:09	700	17-29	344	120	+1.1

^aTime at observation start

^bUmbral start time from JPL NAIF ephemeris

^cThe Jovian sub-Io longitude at mid-observation

^dFor 10° tilt of magnetic pole towards CML 202. Owing to centrifugal stretching, the Jovian plasma torus is tilted 3° relative to the magnetic equator.

with an average dispersion of 1.55 Å/pixel. The corresponding average point source spectral resolution was 3.88 Å (1.41 pixels) and 3.32 Å (2.14 pixels), respectively. For the CCD observations, Io's diameter was 21 pixels or 58 Å. Accounting for the instrumental convolution of Io's circular disk reduces the effective resolution element to 44 Å. For the MAMA observations, Io's diameter was 46 pixels or 71 Å, with an effective extended-source resolution element of 54 Å.

The position angle of Jupiter's pole was -21° and the position angle of the spatial axis of the aperture (the detector y axis) was -157° and -139° on the two dates, respectively. Thus, relative to Jupiter's north pole, the aperture was oriented -136° for the NUV-visible CCD spectra and -118° for the UV MAMA spectra. Jupiter's equatorial radius was 21."1 and 21."9, respectively, on the two dates. Jupiter was tilted 3.26° towards the Sun so the chord of Io's path through the umbra was 0.34 of a Jovian radius north of the umbral center. This path is approximately 12% less than the umbral

Table 2: Configuration

Date (UT)	Detector & filter	Jupiter ^a direction (deg)	Aperture ^b orientation (deg)	Io diameter (")	Solar phase angle (deg)
1999 Aug 7	CCD/G430L	226	-136	1.08	11.63
1999 Aug 7	CCD/G430L	226	-136	1.08	11.63
1999 Aug 18	MAMA/G230L	208	-118	1.12	11.08
1999 Aug 18	MAMA/G230L	208	-118	1.12	11.08

^aPosition angle of Jupiter relative to aperture spatial (y) axis

^bPosition angle of the aperture spatial axis in the Jovian system

diameter, delaying ingress and accelerating egress.

The intensity of the background sky exceeded Io's intensity significantly. The magnitude of excess sky intensity varied as a function of wavelength and increased throughout each eclipse observation as Io's line of sight moved closer to Jupiter. The UV MAMA observations began 1 min after umbral ingress and ended 28 min later, 29 min into the umbra. During this time, Io's projected distance from Jupiter's center changed from 44."4 from to 36."3 (7.3 Io diameters) and the dominating sky background due to scattered Jupiter light increased by up to 40% above 2100 Å. The average sky background for the co-added MAMA observations rose from undetectable to a plateau of 11 R/Å near 2400 Å, then rose to a local peak at 49 R/Å at 2700 R/Å, dipped to 38 R/Å at 2800 Å, then rose through 100 R/Å at 3000 Å. By contrast, the NUV-visible CCD observations began deeper into the umbra, 13 min after ingress, and ended 26 min later, 39 min into the umbra. Meanwhile, Io's distance on the plane of the sky changed from 41."0 to 33."5 (6.9 Io diameters) and the sky background averaged over this band increased by 30%. The sky background averaged over the co-added CCD observations (shown scaled in Figs. 1c and 4) increased monotonically from 100 R/Å at 3000 Å to 900 R/Å at 5700 Å.

3 Data Reduction and Interpretation

The STScI/STSDAS pipeline reduction procedure was applied with updated calibration files to obtain the counts/pixel spectra and wavelength calibration. The STSDAS x2d task was then applied using updated calibration files to convert to spectral images calibrated in intensity units. In addition, the two exposures for each eclipse were co-added into a single spectral image having an improved S/N ratio. All single and co-added reduced spectral images were then median filtered to remove the noise of outlying deviant pixel values from the data and increase the S/N ratio. The data used for fitting the simulations were median filtered once using only a 3x3 pixel median. However, this introduces an error in the zero-point of the sky-subtracted Io spectrum by spatially convolving reference sky strips near the edges of the aperture with instrumentally vignetted rows close to the edge and with rows of Io's nearby disk. To measure the sky background level more accurately, we separately applied a 3x1 median to the unfiltered data that smoothed only in the dispersion direction.

3.1 Extraction Strategy

Although the STIS pixels are capable in principle of providing high spatial resolution, it was necessary to bin them in both dimensions of the spectral image in order to improve the S/N of the observations and thus improve our ability to reliably identify the spectral features above the noise. This binning is in addition to the previously discussed initial 3x3 median filtering. Further improvement in the S/N resulted from extracting 1-D spectra of Io, either over the whole disk or over two halves of Io's disk separately. Comparing Io's half-disk spectra verified the reality of features seen in the whole-disk spectrum, provided information on the quality of the sky subtraction, and constrained the emission gradient over the disk (when the halves were extracted independently). Comparison of the halves alongside the propagated statistical error spectrum also provided an indication of the systematic error. In addition, Io's half-disk spectra were extracted separately for each of the individual and for the combined eclipse exposures. Boxcar smoothing over at least a spectral resolution element (which

is limited by Io's disk diameter) further improved the S/N. For extended sources fully filling the aperture, such as Jupiter's scattered light, the spectral resolution wavelength elements were 108 Å for the CCD and 127 Å for the MAMA detector. In order to merge Io's visible and UV spectra, which have different dispersions, the smoothing box size was adjusted for each detector to yield essentially the same spectral resolution element; 112.5 Å and 110 Å, respectively.

The greatest source of error in extracting Io's spectral image was in the determination and subtraction of the sky background. Owing to the proximity and direction of Jupiter, an oblique sky intensity gradient occurred across the aperture and Io's spectral image. Over the eclipse, the sky background exceeded Io's emission intensity spectral envelope by a factor as high as 9 at 2700 Å for the MAMA observations, and by 25 at 5000 Å for the CCD observations. In order to minimize the sky-subtraction error, we averaged adjacent sky rows near opposite edges of the aperture on either side of Io's disk. The small aperture size, chosen to minimize scattered light from Jupiter, severely limited the number of rows on either side of Io available for averaging the scattered Jovian spectrum. In selecting the detector rows to define the background, we made allowance for aperture vignetting, potential mis-centering of Io in the aperture, and emission extending beyond Io's limb. Differences in the properties of the two STIS detectors and in Io's spectrum over the different wavelength regimes necessitated different procedures for extracting spectra for the CCD and MAMA observations. These detailed procedures and the effective apertures for extracting spectra are described separately for each detector in the Appendix.

Io's spectrum was extracted from the observed spectral images by subtracting Jupiter's foreground scattered spectrum. In order to estimate the scattered light level in each row associated with Io's disk and extended emission, we interpolated spatially the average background intensity observed on each side of the disk. The spatial interpolation was done along each wavelength column. Linear interpolation was adopted as there was no clear constraint on the background curvature, given the small size of

the aperture. In the case of Io's whole-disk extractions, two methods were used and applied to both detectors. The direct method was to sum the resulting spectral image over the intervening rows to extract Io's whole-disk 1-D spectrum including extended emission. An alternative method of obtaining Io's whole-disk spectrum was simply to combine spectra of Io's extracted halves; however, this method captures less of the extended emission owing to the smaller effective aperture used (see the Appendix for details).

Emission from Io has been observed to extend at least to 1" beyond the disk. This is thought to arise from high altitude excitation from the Jovian plasma torus. Determining the spatial distribution of this faint emission from Earth is difficult owing to its proximity to bright Jupiter in the night sky. Only emission falling within the effective detector aperture was included in the extracted spectrum. For the complementary half-disk spectra, essentially only those rows that are on the disk are spatially co-added, whereas for the extended whole disk spectra rows are included that are beyond the disk diameter to allow investigation of any emission that extends beyond the diameter of Io's disk. For the CCD, when Io's diameter was 1."08, the effective aperture extracted for Io's whole-disk spectrum was 2."03 x 1."58. This was 41% larger (in the spatial dimension) than the aperture used for comparing the Io halves; namely, 2."03 x 1."12. For the MAMA detector, when Io's diameter was 1."12, the effective aperture extracted for Io's whole-disk spectrum was 2."03 x 1."51. This was 32% larger than the aperture used for comparing the Io halves; namely, 2."03 x 1."14. For a map of the effective apertures and sky strips for each detector, see Fig. A1 in the Appendix. Owing to the uncertainty in the distribution of Io's emission over the effective aperture, the extracted emission flux was referred to the solid angle of Io's disk to yield an equivalent disk-averaged intensity spectrum that can be compared to future investigative results. The intensity units were converted to Rayleighs/Å, where 1 Rayleigh corresponds to 1×10^6 photons $\text{cm}^{-2}\text{s}^{-1}$ per 4π sr.

The directions NE and SW, which refer to the detector's spatial axis with North

in the Jovian system projected onto the plane of the sky, are only approximate. They differ by 18° for the CCD and MAMA observations. The actual orientations are given in Table 2. NE refers to the lower half of the detector (lower row numbers) and SW refers to the the upper half. Since Io was west of Jupiter, NE was the closer half to Jupiter in the plane of the sky, hereafter the “Jupiter-approaching” side for short. Unless explicitly indicated otherwise, the propagated statistical error spectrum on the plots always represents the $1-\sigma$ standard deviation. It includes the contribution from subtracting the sky spectrum, but excludes systematic effects. The sensitivity of each detector declines noticeably towards longer wavelengths.

3.2 CCD Spectra

Independently extracted spectra of Io’s NE and SW halves are shown in Fig. 1a for two spectral resolutions, 112 \AA (41 pixels; upper panel) and 59 \AA (21 pixels; lower panel). These are based on the average two consecutive STIS/CCD observations taken during the eclipse of Aug 7, 1999. These spectra are independent in the sense that a different sky spectrum was subtracted from each Io half. However, their zero level is uncertain owing to the intensity gradient of the background across the aperture and the adjustment of the sky level to superpose the complementary extracted halves conveniently for close comparison of their features. These and other spectra reported in this paper that apply to Io’s half disk were extracted from a region of the STIS aperture restricted in the spatial dimension by Io’s projected diameter (see the aperture geometry in Appendix Fig. A1 for further details). Each spectrum includes the emission from Io’s half disk plus any extended emission lying in the corresponding area of its half aperture. The intensity scale assumes that all the emission observed in each restricted aperture half arises uniformly over that half of Io’s disk. There is rough agreement between corresponding pairs of stronger features above 4100 \AA common to both halves of Io. The agreement between the independent Io halves extends to higher spectral resolution, despite the accompanying lower S/N ratio. The strongly smoothed features are seen to resolve into multiple narrower features that correspond across Io, lending

support to their reality. They cannot all be caused by artifacts in the sky spectrum that similarly affects both extracted halves. The intensity divergence at longer

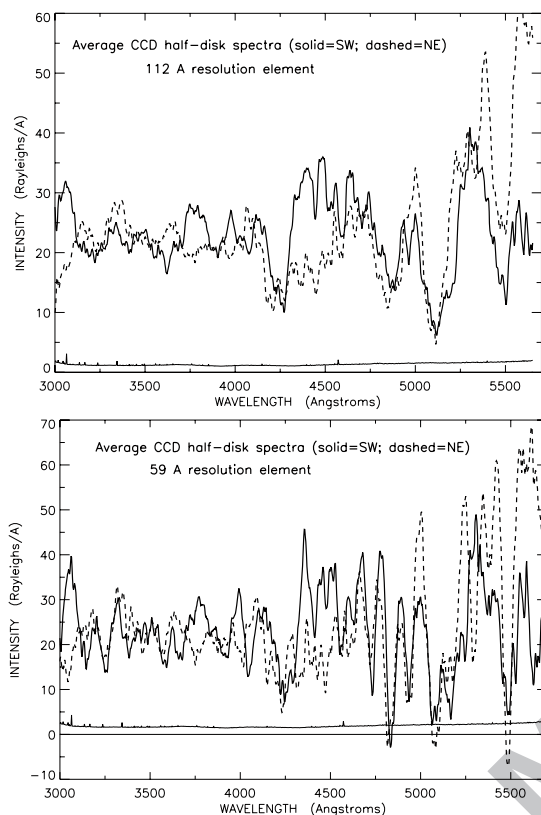


Fig. 1a: Independently extracted spectra of Io’s NE and SW halves (see precise orientation in Table 2) that average two consecutive CCD eclipse observations taken on Aug 7, 1999, when Io was on the west side of Jupiter. The two panels are the same except that the lower has half the box-car smoothing. The agreement of the stronger spectral features common to complementary halves of Io’s disk for the two spectral resolutions shown indicates they are likely real. The $1\text{-}\sigma$ propagated statistical error is also plotted for the combined halves, scaled by $\sqrt{2}$ to represent the error for the halves.

wavelengths, however, likely indicates systematic error in the sky subtraction.

With the reality of the prominent features above 4100 \AA now established, the condition that the extracted halves be independent is hereinafter relaxed in order to increase the useful extracted spectral resolution. The upper panel of Fig. 1b compares the corresponding dependently extracted spectra using a resolution element of 31 \AA (11 pixels). Because the sky is now linearly interpolated across Io’s disk, the extracted spectral halves are no longer independent. The improved feature visibility results from averaging twice as much sky area, as well as from the increased resolution. The spectral halves have deliberately been left unbalanced in order to compare their brightnesses. The spectrum appears to be brighter on the NE or (obliquely) “Jupiter-approaching” half of Io. Several significantly brighter features above 4900 \AA appear on the NE side. The comparison shows continued correspondence in wavelength for most newly resolved features. This spectrum suggests emission from a molecular species.

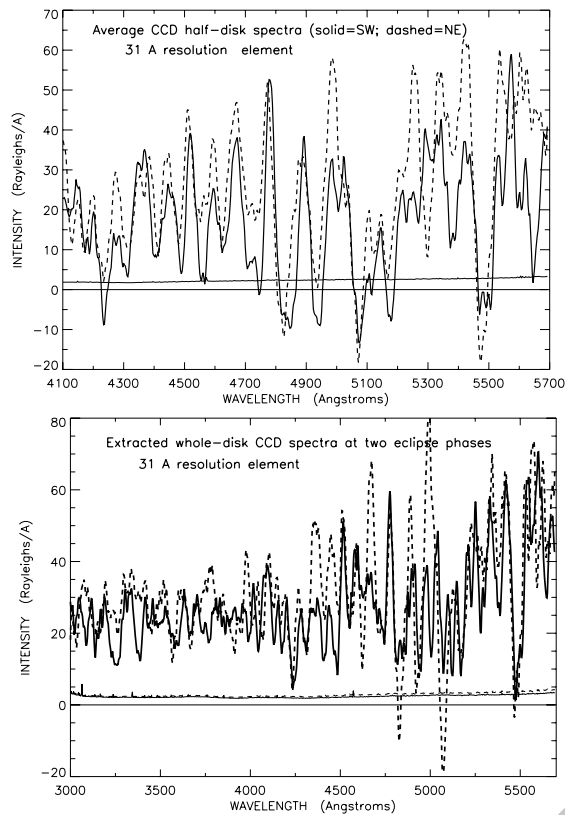


Fig. 1b: Dependently extracted CCD spectra of Io's NE and SW halves, for which the sky background spectrum was interpolated across Io's disk before subtraction. The upper panel compares spectra of Io's NE and SW halves above 4100 Å that are no longer independent nor artificially balanced. The agreement of feature wavelengths between the halves is nearly total over this interval, with mostly brighter emission on the NE side. The lower panel shows whole-disk CCD spectra of Io at two umbral phases on 7 Aug. The two most-negative dips seen in the second spectrum (dashed) are apparently noise since they are not matched in the first exposure (the solid line). The sky zero level for this extracted spectrum was adjusted to avoid other negative data.

The lower panel of Fig. 1b compares the whole-disk CCD spectra of Io extracted at the two separate umbral phases of the same eclipse (Table 1). The solid spectrum is for the earlier exposure. The correspondence of the matching features is evident in wavelength, if not in intensity. No correspondence was detected between the spectral features and fringing in the spectral image for either eclipse exposure. These temporally independent spectra were constructed by averaging dependent spectra of Io halves extracted from the respective observations using the smaller effective aperture. Plots of these individual halves (not shown) were found to mimic their whole-disk counterparts at each CCD eclipse phase (and they confirm that the NE side is brighter). The sky/Io spectral intensity ratio is proportionately greater for the larger extraction aperture and greater for the second eclipse exposure. Io's extracted CCD spectrum divided by the sky spectrum is shown in Fig. 1c for the two eclipse phases. This intensity ratio shows the increasingly dominating role of the sky background in the extraction up to 4100 Å. Since the sky subtraction is the greatest source of statistical and systematic error, the

noise is greatest and the zero level is least certain for Io's extracted spectrum above this wavelength. The two most negative dips in the later spectrum (dashed line) of lower Fig. 1c are apparently artifacts of noise since these outliers are not evident in the spectrum exposed only a few minutes earlier (solid line), which has a higher S/N

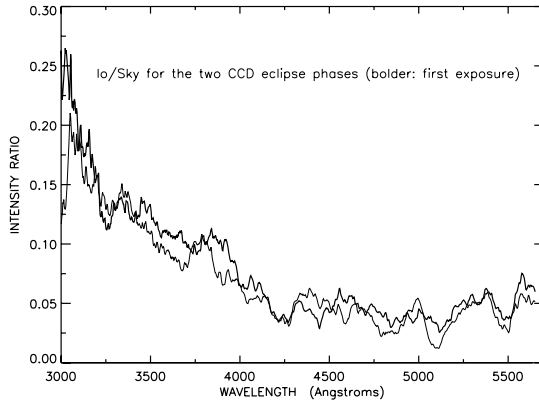


Fig. 1c: Comparison of the sky background spectrum divided by Io's spectrum extracted at spectral resolution element 112 \AA for the two separate CCD eclipse observations. The bolder spectrum is the first observation. The sky zero level has been corrected as discussed in the text. The sky background increasingly dominates Io's spectrum with increasing wavelength.

owing to the lower sky background at Jupiter's greater angular distance. The zero level in the lower panel was accordingly adjusted downward relative to Fig. 1a and to the upper panel of this Figure to avoid negative values in the rest of these data. This was done by adjusting hereinafter the zero level of the sky background before its subtraction.

Upper Fig. 1d shows the unidentified emission with the propagated error spectrum extracted over the whole disk through the larger effective aperture, so it includes more extended emission. Both exposures were co-added to improve S/N. The zero level of the background was again adjusted to avoid negativity, ignoring the noise artifact dipping below -10 R/\AA just below 5100 \AA . This corresponds to the similar adjustment for the separate eclipse exposures shown in lower Fig. 1b for the smaller effective extraction aperture. With its higher S/N and corrected zero level for the subtracted background, Fig. 1d is the one to use for comparison with laboratory spectra for species identification and modeling.

The lower panel illustrates the lack of correspondence between Io's unidentified spectral features and the sky background. Io's combined whole-disk CCD spectrum (dashed) is overplotted on the scaled Jovian scattered light background spectrum,

“Avg Sky” (thick), which is the average of the background observed on each side of Io’s disk. No correlation with Io’s spectral features is evident. “Sky Difference” (lower thin) plots the difference of those sky strips, which is positive due to the background gradient. The indicated percentages refer to the amount of intensity scaling applied to facilitate comparison. A rough correlation between the sky difference and Io’s emission is suggested in the lower plot between 4300–4900 Å although not at other wavelengths.

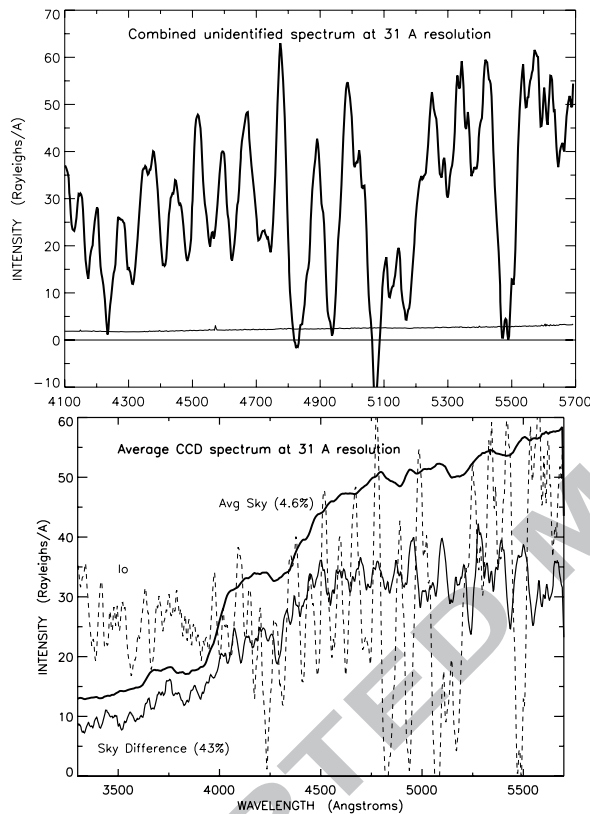


Fig. 1d: Upper: Combined, background zero-adjusted, larger-aperture spectrum for the unidentified emission with $1\text{-}\sigma$ propagated error (The $-10\text{ R}/\text{\AA}$ dip appears to result from a noisy pixel). The lower panel shows lack of correspondence between Io’s extracted whole-disk spectrum (dashed) and the averaged Jovian scattered light background spectrum, scaled to permit comparison: “Avg Sky” (scaled by 4.6%, thick) is the average of the background in the aperture on each side of Io’s disk. “Sky Difference” (scaled by 43%, thin) plots the difference of those sky strips, which is positive due to the background gradient.

This probably indicates sky contamination by Io’s asymmetrically distributed unidentified emission, which is brighter on Io’s NE side. Jupiter’s spectrum cannot explain these features because there is no hint of them in the Avg Sky spectrum, which is only 14 times brighter than Sky Difference here. Differential fringing across the detector is an unlikely cause since such fringing is not observed in the scattered Jupiter spectrum. Periodicity in the dark image has not been observed.

The upper panel of Fig. 1e shows the combined Io spectrum of Fig. 1d replotted onto a frequency scale in preparation for a Fortrat plot with the consecutive emission peaks marked from #1 on the right to #17 on the left. Peak #13 is questionable

because it is weak and poorly defined. The lower panel shows a Fortrat diagram plotting the frequency of the emission features marked above vs. sequence number. All emission peaks are seen to lie close to a linear progression, with no indication of curvature. This indicates a linear progression of the transition energy with quantum number, with average band spacing of 404.5 cm^{-1} . This spacing excludes a rotational progression since this would correspond to a rotational constant of 203 cm^{-1} while most such constants lie below 15 cm^{-1} . For the ground electronic and vibrational state of H_2 , the lightest molecule with the smallest moment of inertia, the rotational constant is only 61 cm^{-1} . We conclude that the progression, which extends over at least 0.8 eV , represents a vibrational series of an electronic band.

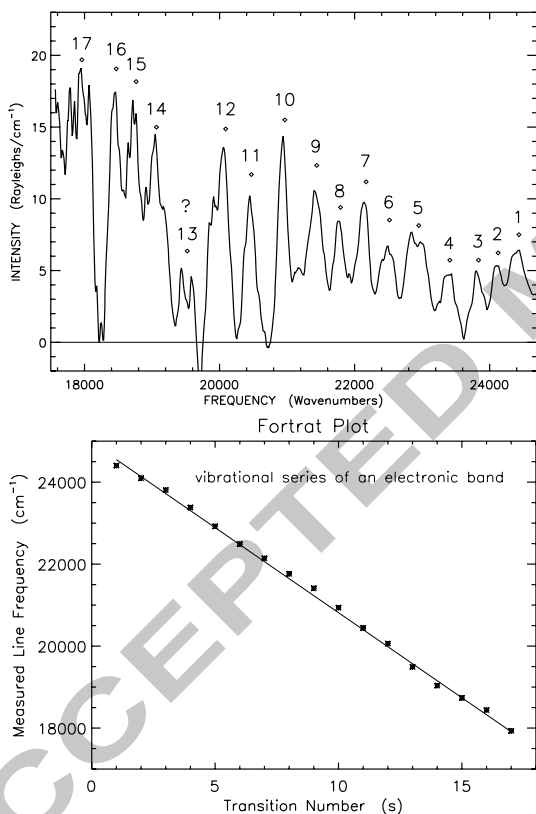


Fig. 1e: Upper: Io's whole-disk spectrum replotted onto a frequency scale with the emission peaks marked. Peak #13 is uncertain; its absence might help diagnose the series. Lower: Fortrat plot of the frequency of the emission peaks marked above vs. the transition number, which has an arbitrary zero point and sign. All emission peaks are seen to lie close to a linear progression, with no indication of curvature. The 0.8 eV range and spacing of the series indicates emission from a vibrationally excited electronic band.

3.3 MAMA Spectra

Turning to the NUV spectra obtained with the STIS/MAMA detector, we found that sky subtraction for the MAMA leads to a mostly lower S/N than for the CCD spectra so we adjusted the normalization of the extracted MAMA spectra to be continuous with the extracted CCD spectrum. This is reflected in the plots below. This

continuity is needed for fitting a model SO_2 spectrum because its emission spans both spectral regimes. This should be satisfactory so long as Jupiter’s scattered spectrum has been fully subtracted on the two eclipse dates, but neglects any differential freezing out of Io’s atmosphere during the early umbral phases observed for each eclipse. Since each pair of Io halves spectra for the MAMA observations were balanced to facilitate close comparison of spectral features, they do not reliably indicate which side of Io

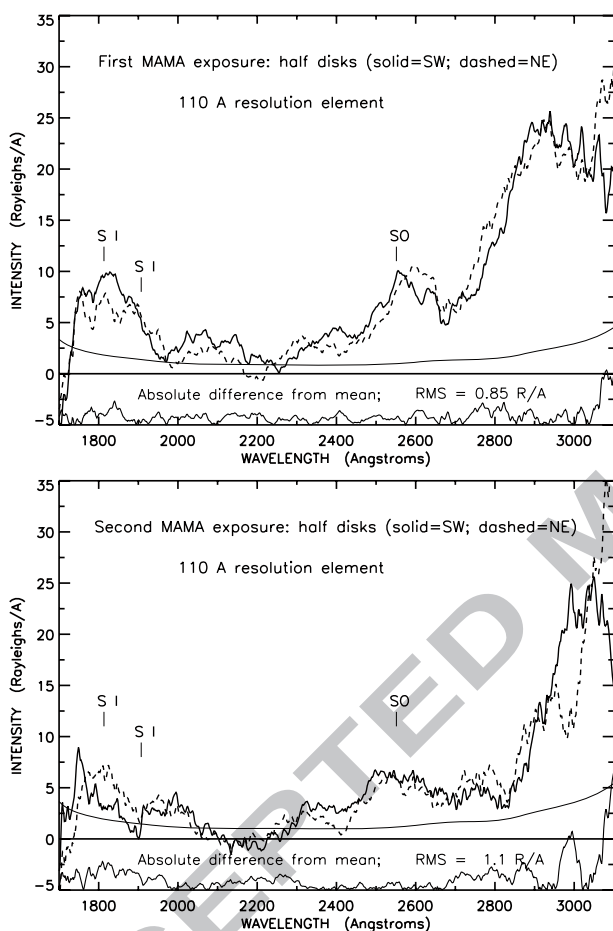


Fig. 2a: Comparison of sky-subtracted spectra of Io’s NE and SW halves taken during each of the two consecutive STIS/MAMA detector exposures of Io’s early umbral eclipse on Aug 18, 1999. These extracted half-Io spectra have been boxcar smoothed over 71 pixels to give a spectral resolution of 110 Å. They are linearly dependent since their extraction interpolates sky. The Io halves are symmetrical, verified here *a posteriori*. The spectra are normalized approximately to match the whole-disk, eclipse-average, CCD spectrum over 3000–3100 Å for continuity. Offset below (by 5 R/Å) for each panel, the absolute value of half the difference between the half-disk spectra is plotted for comparison. “RMS” gives the standard deviation of this difference over the spectral interval 1760–3000 Å, avoiding elevated noise. The upper panel compares Io halves for the first exposure of the eclipse and the lower panel compares the halves for the second exposure, which appears broadly weaker between 2500–3000 Å.

is brighter. In terms of extracting Io’s spectrum, the sky background is unimportant below 2100 Å and is negligible below 2000 Å. At the SO peak emission at 2550 Å and near the SO_2 peak at 3000 Å, the sky intensity is, respectively, only 2.0 and 3.7 times brighter than Io for the averaged MAMA observations. Overall, the sky subtraction is less critical than for the CCD extractions.

Figure 2a shows, respectively, the sky-subtracted spectra of Io’s NE and SW halves taken during the first and second consecutive MAMA detector exposures of Io’s early

umbral eclipse on Aug 18, 1999. These extracted spectra have been boxcar smoothed over 71 pixels to give an effective spectral resolution of 110 \AA . The extent of the agreement between the extracted halves supports the reality of the broader features. For close comparison, the sub-panels plot the absolute value of half the difference between these two spectra (i.e., the absolute difference from the mean). “RMS” gives its empirical standard deviation over the spectral interval $1760\text{--}3000 \text{ \AA}$. The $1\text{-}\sigma$ statistical error is also plotted. The NE (dashed) spectrum of the second exposure was offset by $+1.4 \text{ R/\AA}$ to avoid negativity at 2200 \AA resulting from an uncertain dark current subtraction and to compare Io halves (The dark current appears to have been different between the sky background and Io rows). This appears to be justified by the broad agreement across the spectral range of the halves after offset (after allowing for the falling MAMA sensitivity at longer wavelengths). Although the Io halves spectra agree fairly well at each eclipse phase, there is significant disagreement between the phases.

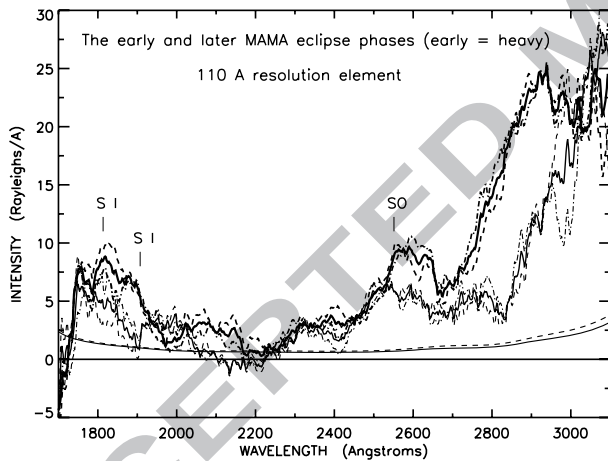


Fig. 2b: Temporal change of the Aug 18, 1999 eclipse observed with the MAMA detector, beginning a minute after umbral ingress. The half-disk spectra of Fig. 2a at each eclipse phase are plotted here for temporal comparison. Also, their whole-disk averages have been overplotted as thick lines (the earlier phase is plotted bolder). The dot-dashed spectra represent Io’s NE half and the dashed spectra Io’s SW half. The $1\text{-}\sigma$ error curves (thin) represent the whole-disk averages, with the dotted curve corresponding to the later observation.

The second phase is broadly weaker, especially between $2500\text{--}3000 \text{ \AA}$, although the phases are normalized the same. The 40% higher sky background during the second exposure would contribute to the disagreement, as would changes in Io’s atmospheric column or excited SO production (see below).

Since the eclipse observed with the MAMA detector is the only observation that captured the early umbral phase, it has the best leverage for assessing temporal change.

Therefore, the spectra of Fig. 2a and their whole-disk averages (bold lines) are re-plotted in Fig. 2b to enable a direct temporal comparison of the two phases. The $1\text{-}\sigma$ error curves shown represent only the statistical error for the whole-disk averages. The corresponding error for the halves is approximately $\sqrt{2}$ larger. Io's emission

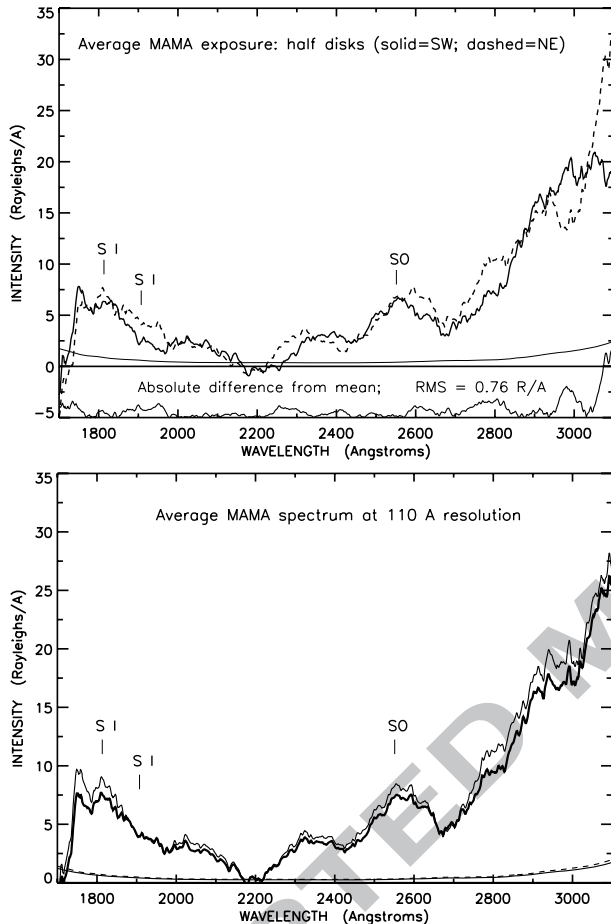


Fig. 2c: Upper: Io halves spectra for the average of the consecutive STIS/MAMA exposures taken during Io's umbral eclipse on Aug 18, 1999. These halves are time-averages of the respective halves shown in Fig. 2a, and so include all the available exposures up to 29 min. post eclipse ingress. Lower: Whole-disk spectra of Io co-added over this umbral eclipse. The bold spectrum averages the Io halves spectra of the top panel. The plotted spectra are emission spectra derived from averaging over the whole disk, using only on-disk emission (bold); and the emission spectra that results from on-disk emission plus emission extended beyond the disk (light). Comparison of these spectra provides a constraint on the extent of Io's emission. The dashed $1\text{-}\sigma$ error spectrum corresponds to the larger aperture.

spectrum appears to have generally weakened during eclipse. The difference between the eclipse phases is typically greater than the disagreement between the disk halves at each phase, particularly for the SO and S I emission, although the corresponding halves are dependent. The greater difference in the emission between 2800–2950 Å is likely due to excessive dark subtraction by the data reduction pipeline in the later exposure, as indicated by its negative dip at 2200 Å. This would cause an error in the calibrated intensity that increases with intensity, in this case depressing the spectrum. So some of the depression is instrumental rather than temporal change. Adjusting the dark to force agreement at 2900 Å would have caused a mis-fit between the two phases at 3100

Å. So at least some of the MUV 1 temporal weakening deeper into eclipse indicated in this Figure is real. The systematic error prevents a more quantitative separation of the temporal changes from instrumental effects.

In the case of the extracted whole-eclipse spectra shown in Fig. 2c for the co-added halves and the whole disk, there was enough S/N that after correction of the residual negativity at 2200 Å, Io's merged spectrum reproduced the slope of the blue wing of the lab SO₂ spectrum (shown below in Fig. 4). This whole-eclipse, whole-disk spectrum is used in constraining our simulation because it is the most reliable; it has the highest S/N ratio and the least systematic zero offset error. The lower panel shows Io's whole-disk spectrum, again averaged over both MAMA eclipse exposures. The bold spectrum averages the above Io halves spectra. The light spectrum applies the same scaling but extracts Io's whole disk over an effective aperture that is 32% larger in the spatial dimension. The result is emission that is up to 1–2 R/Å brighter. The dashed error spectrum corresponds to the larger aperture.

Figure 3 shows Io's spectrum extracted with a spectral resolution element 39 Å (25 pixels) from the dark-corrected average of the two consecutive eclipse MAMA exposures taken during Io's early umbral eclipse on Aug 18, 1999. The extracted spectrum is unreliable below 1750 Å due to the low signal level. The thick solid line represents Io's whole disk, sky-subtracted spectrum. This is taken to be the corresponding average of complementary half-disk spectra, which are also shown. Laboratory SO₂ dissociative excitation cross sections of SO₂ (e.g., Ajello et al. 2002) extend down only to 2000 Å. However, a pair of laboratory spectra showing S I lines in emission is shown offset (Ajello, personal communication), which were generated by 25 and 200 eV electrons impacting SO₂ vapor (the brighter is 200 eV). These show that the line ratio depends on electron energy. These have been broadened by convolution with Io's disk, assuming uniform emission, and have a common arbitrary scale (The convolution matters only when the applied smoothing is less than 60 Å). Corresponding S I emission features are seen in Io's spectrum, complementing Clarke et al.'s (1994) detection of S and O

lines in Io's FUV spectrum. The communicated spectra are valid only for a specific set of laboratory conditions and so are not suitable for fitting to Io's spectrum.

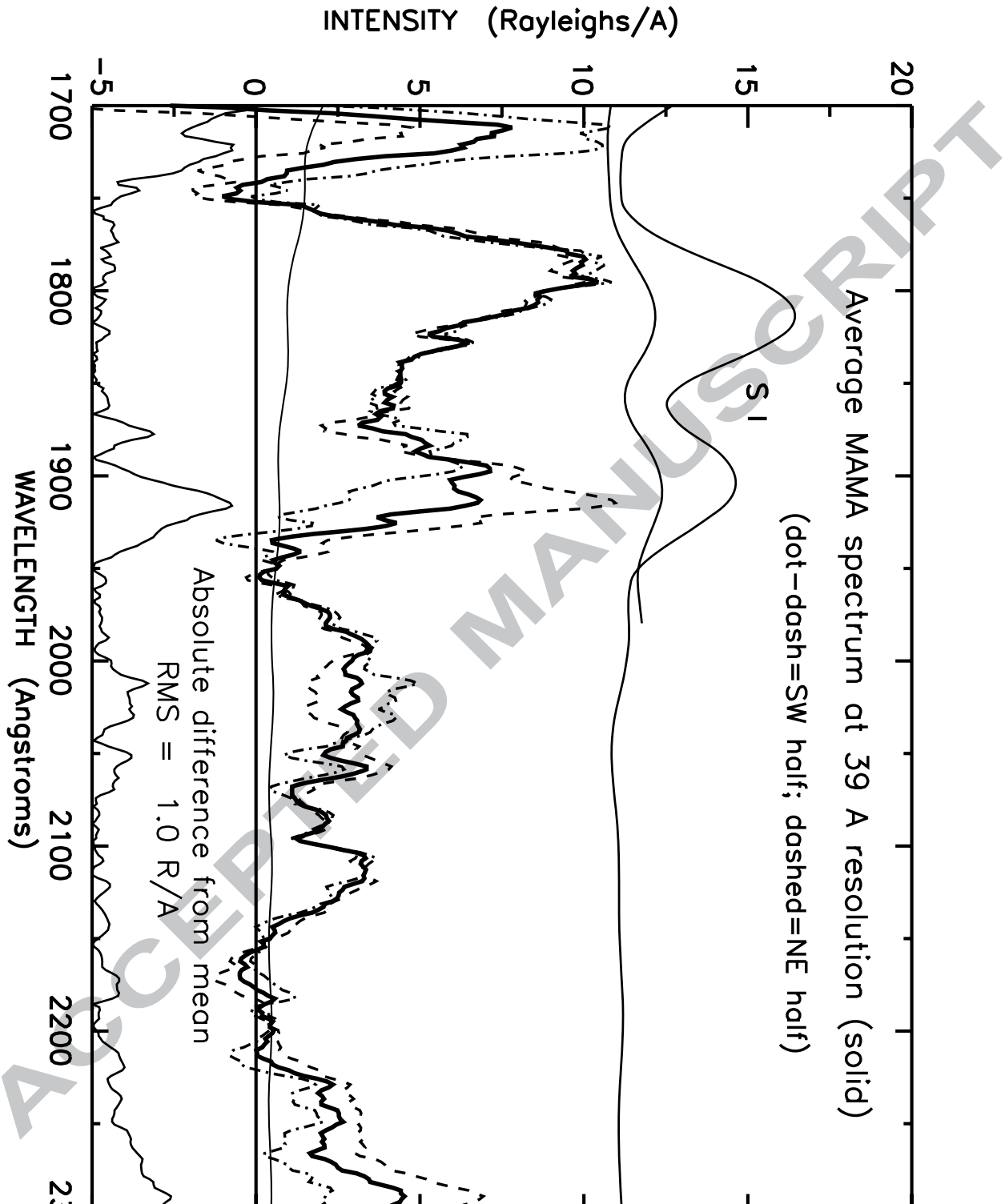


Fig. 18. Average of sky-subtracted whole-disk spectra of Io taken during Io's early umbral eclipse on Aug 18, 1999 extracted at spectral resolution element 39 Å (25 pixels). The thick solid line spectrum is for Io's whole disk averaged over the

two MAMA eclipse exposures, which is taken to be the average of the corresponding complementary half-disk spectra, which are also shown. An arbitrarily-scaled pair of laboratory spectra showing S I emission lines generated by 25 and 200 eV electrons, respectively, impacting SO₂ vapor is shown offset by +11 R/Å (the brighter is for 200 eV) (Ajello, personal communication). The corresponding S I emission is evident in Io's eclipse spectrum. The empirical "RMS" value is the standard deviation of the difference spectrum over the interval 1800–2300 Å.

The jump in the absolute difference of the feature at 1915 Å relative to the rest of the reliable region of the spectrum (>1750 Å) suggests that the difference in this feature between Io's NE and SW halves is real, with the emission being brighter on the Jupiter-approaching (wake) side of Io. The fact that the shorter wavelength multiplet is allowed while the other is dipole forbidden may play a role in the sensitivity of this ratio. Different excitation conditions on opposite sides of Io might affect the 1915 Å multiplet preferentially. The lab data are inadequate for fitting these features and simulating them is outside the scope of this paper.

3.4 Merged Spectra

Figure 4 shows Io's merged whole-disk, eclipse-averaged, extracted spectrum from the smaller aperture plotted with resolution element 110–112 Å. The sensitivity to varying the sky background by $\pm 0.7\%$ in extracting Io's CCD spectrum is also shown to be least at the shortest CCD wavelength, close to the laboratory SO₂ "MUV 2" emission peak near 3150 Å (following the nomenclature of Ajello 1992), reducing the uncertainty in fitting models of the SO₂ spectrum. Io was close to the torus equator during the MAMA eclipse observations and near the torus edge during the CCD exposures, where the electron flux is somewhat less. The middle (nominal) CCD spectrum was used to adjust the normalization of the extracted MAMA spectrum by matching at their overlap. This removed any intensity discontinuity arising from the different eclipse phases and magnetic latitudes of Io on the two dates, which allowed simulating the emission spectrum. Also plotted for comparison are the subtracted sky spectrum (dots) and Io's bright daytime continuum spectrum (dashes), both arbitrarily scaled to the upper spectrum at 5700 Å. The lack of correspondence between broad features of the sky spectrum and Io's extracted spectrum confirms the sky subtraction. The

scaled daytime continuum spectrum was derived from Io's trailing geometric albedo spectrum observed by Wamsteker (1972) and Allen's (1976) visible solar flux spectrum. Since Allen's spectrum is smoothed over 100–500 Å, which exceeds the disk-convolved resolution element of Io's spectrum, spectral detail is lacking with which to make a direct comparison with the data. However, we conclude that the solar contribution to the NUV-visible CCD extracted spectrum below 3000 Å is negligible because: 1) during eclipse Io is not directly illuminated by solar light and 2) based on the Cassini observations of Io in eclipse (Geissler et al. 2004), the contribution from refracted sunlight is expected to be low (see the detailed arguments in the Discussion). For comparison, scaled laboratory spectra of SO₂ at 9 eV and 11 eV are overplotted (the pair of light lines; Ajello et al. 2002). These differ essentially only in the neighborhood of the SO emission, bracketing it. The rough fit shows agreement on the blue wing of the laboratory spectrum with Io's observed spectrum between the SO feature and the emission peak. There is a big disagreement above 3300 Å, even if the sky is scaled over the range indicated before subtraction, indicating the presence of another emitting species. These laboratory spectra are only roughly indicative because of their narrow exciting electron energy range; proper fitting requires a full simulation.

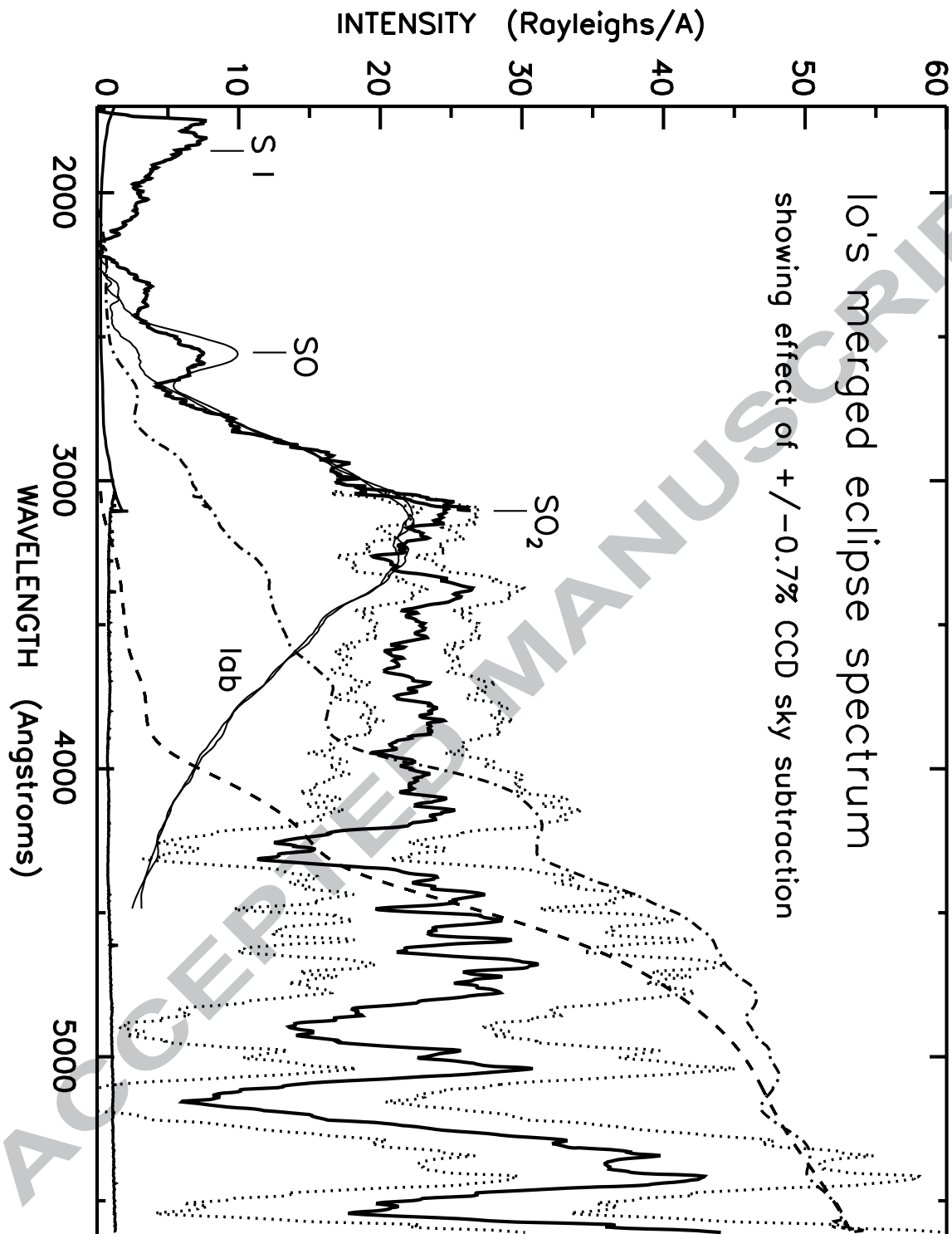


Fig. 4: Io's merged, whole disk (combined halves), eclipse averaged, spectrum (bold). The large effect of varying the sky background by $\pm 0.7\%$ in extracting Io's CCD spectrum is indicated by the bracketing dotted spectra. The respective $1-\sigma$ propagated statistical error spectra for Io's nominal spectrum are plotted near the bottom (shallow concave solid lines). Also plotted for comparison are two nearly

overlapping scaled laboratory spectra for SO_2 excited by impact of electrons at 9 eV and 11 eV (thin lines peaking near 3150 Å and bracketing the observed SO band; Ajello et al. 2002). These show the sensitivity to electron energy at the SO band although not actually fitted to the data. Further shown are Io's daytime continuum spectrum (dashes) and the subtracted sky background spectrum (dot-dash) (Allen 1976), both arbitrarily normalized to the upper dotted spectrum at 5700 Å. The plotted daytime spectrum shows that Io's continuum spectrum in eclipse is negligible throughout the MAMA wavelengths and below 3300 Å in the CCD spectrum. The lack of correspondence between Io's extracted spectrum and the sky spectrum demonstrates the degree of success of the sky subtraction. See text for details.

Figure 5 (upper) shows the average of the two CCD eclipse observations taken in early Jovian umbral eclipse on Aug 7, 1999 and extracted through the two effective apertures. The bold spectrum combines spectra of Io halves through the smaller effective aperture and the light spectrum is the whole-disk extraction, which has a 50% larger effective aperture in the spatial dimension. Ideally, the average of these spectra would correspond to the average of the spectra in Fig. 1a. The difference is due to different extraction methods in order that the halves of Fig. 1a be independent.

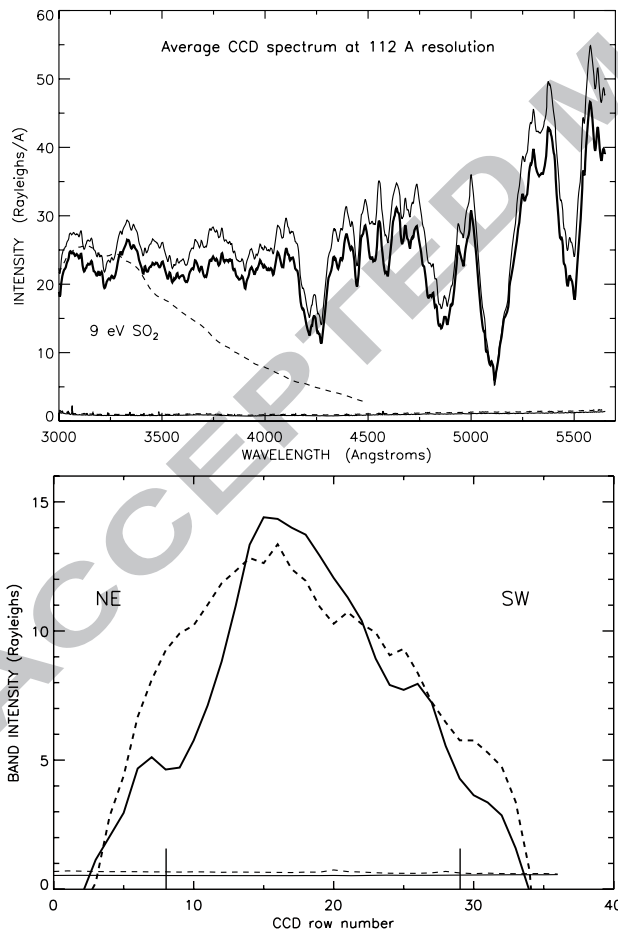


Fig. 5: Evidence for Io's extended emission. Upper: Average of two consecutive STIS/CCD detector exposures of Io's early umbral eclipse on Aug 7, 1999. The bold spectrum combines spectra of Io halves and the light spectrum is the whole-disk extraction, which has a 50% larger effective aperture. The sloped dashed curve peaking near 3150 Å is the lab spectrum for dissociative excitation of SO_2 by 9 eV electron impact, arbitrarily scaled. Evidence of relatively extended emission is apparent, both for SO_2 near the peak and for the unidentified species above $\sim 3700\text{Å}$. The $1\text{-}\sigma$ propagated statistical error for Io is plotted below (dashed for the whole-disk extraction). Lower: Intensity profiles of Io's SO_2 (solid; averaged over 3009–3750 Å) and unidentified (dashed; averaged over 4108–5673 Å) emission vs CCD row number. Each row pixel is $0.05''$. Io's center is at row 18 with the disk lying between rows 8 – 29 (vertical lines). The data have been boxcar-medianaed over 3 rows. The $1\text{-}\sigma$ propagated statistical error is plotted below (dashed for the unidentified emission).

The propagated statistical error is plotted below (dashed for the whole-disk extraction). The above-mentioned artifact pegs the core of the 5100 Å feature at the same value for both apertures (see lower Fig. 1b). This Figure shows extended emission across the plot; i.e., for SO₂ on the left (represented by the dashed line below 4500Å) and for the unidentified species above and to the right of the dashed line, ramping up as the SO₂ emission falls off.

Figure 5 (lower) plots the emission profiles across Io's disk for the unidentified emission averaged over 4108–5673 Å and the SO₂ emission averaged over 3009–3750 Å. The profile for the unidentified emission follows that for SO₂ in the SW half of Io and they peak together, with similar strength, at 0.1 NE of Io's center. However, they diverge after that with the unidentified emission projecting considerably brighter than the SO₂ emission approaching the NE limb. The SO₂ is only mildly brighter in the NE half, almost symmetrical with respect to the peak. Since the NE half represents the Jupiter-approaching side of Io, the unidentified emission may thus be associated with Io's wake spot (Retherford et al. 2000) while SO₂ may be more associated with the active plumes.

4 Analysis

The greatly weakened solar EUV twilight illumination during early eclipse produces negligible emission from photo-excitation and insufficient photoelectrons to generate noticeable SO₂ emission. The emission is therefore dominated by electron impact from the Jovian plasma torus, simplifying analysis, though some residual photoelectrons may still be present during early eclipse. Moreover, such analysis is facilitated by available laboratory spectra generated by the electron impact excitation of SO₂ and its dissociation products at various electron energies (e.g. Ajello et al. (1992a,b; 2002).

4.1 Method

In order to simulate Io's eclipse MUV spectrum from ~2400 to 6000 Å that is generated

via electron impact of the atmosphere, we use our Monte Carlo electron transport code previously applied to simulating Io's [O I] 6300 Å and [S II] 6716 Å aurora (Moore et al., 2010a). Figure 6 shows a schematic of the overall simulation method. The code can compute both the electron and excited neutral dynamics; the model explicitly ignores photo-reactions since Io is in eclipse. The electron guided center motion is simulated in pre-computed magnetic and electric fields (Combi et al., 1998). During each time step, the representative electrons move along the magnetic field lines and drift due to the electric field (see Section 2.2.2 in Moore et al., 2010a for further details). After each move step, the electrons probabilistically collide with the local neutral gas; this procedure is described in more detail below. Excited neutrals (e.g. [O I]) move and collide in a static neutral background atmosphere and can de-excite through collisions (quenching) or spontaneous emission. Neutral gas dynamics and chemistry are included only in the sense that we utilize a prescribed, pre-computed atmospheric model which included these effects. A pre-computed neutral atmosphere ($\text{SO}_2/\text{O}/\text{SO}/\text{S}/\text{O}_2$) composed of a set of active volcanoes super-imposed onto a sublimation atmosphere is used to compute the electron-neutral and excited neutral-neutral collisions. The SO_2

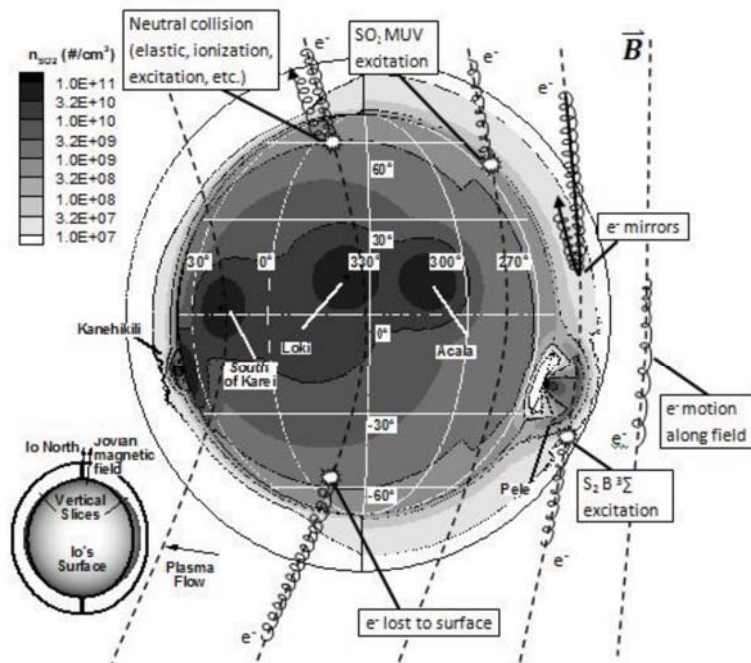


Fig. 6: Schematic representation of the electron transport model. Io is shown with SO_2 density contours at the surface and in radial slices near each limb. The plasma flows from right to left in the schematic and the dashed lines are the

Table 3: Active volcanoes visible during observations

Plume	Longitude	Latitude	Type
Kanehikili	38W	16S	Day Prometheus
Masubi	55W	44S	Day Prometheus
Tvashtar ^a	125W	59N	Night Pele
Pele ^a	256W	20S	Night Pele
Dazhbog ^a	302W	54N	Day Pele
Acala	336W	11N	Day Prometheus
Surt ^a	338W	46N	Day Pele

^aActivity varies depending on simulation case.

distorted and compressed magnetic field lines upon which the electrons move. Note that the electron transport code only computes the guided center motion of the electrons (solid arrow on the upstream electron mirroring off the increased magnetic field) since the Hall parameter is large (>10) and the gyration radius (<10 m) is small compared to relevant atmospheric scales (>1 km). If an MUV excitation occurs then a photon is generated randomly from the appropriate spectra based on the incident electron energy.

density at Io's surface (and in radial slices off Io's limb) used for the current simulations can be seen in Fig. 6. The sublimation atmosphere neutral densities of Wong and Smyth (2000) are adjusted to account approximately for both the effect of eclipse and a lower (daytime) sub-solar temperature of 115K in our calculations which yields a model sub-solar density in better agreement with the observations of Feaga et al. (2009). The simulations super-impose two general types of plumes (each either day or night) pre-computed using Zhang et al.'s (2003a,b, 2004) volcanic model: a Pele type for plumes with a ring radius near ~ 400 km and a Prometheus type for the smaller plumes with a ring radius near ~ 120 km. In order to determine which volcanic plumes were active during the observations, we used Geissler et al.'s (2004) timeline of major eruptions during the Galileo mission. The visible plumes included in the model, and their type (day/night, Pele or Prometheus), are listed in Table 3. For more detail on the model's neutral atmosphere, see Section 2.1 in Moore et al. (2010a).

Our electron transport code determines whether an electron-neutral collision occurs, the neutral species with which the electron interacts, and the collision (interaction) type all in a Monte Carlo fashion by comparing collision probabilities to (pseudo) random numbers. In practice, only one random number is needed per electron per time step to determine what type of collision, if any, occurs. In order to simulate the MUV spectrum, cross section and spectral data provided by Ajello were used to determine if an SO₂ MUV excitation collision occurred and, if so, what wavelength photon was spontaneously emitted. The energy dependent cross sections were obtained via curve-fits to Ajello et al.'s (2002, Table 2) data at many incident electron energies (Moore et al., 2010a Section 2.2.3).

Representative spectra at incident electron energies of 9, 11, 12, and 18 eV are shown in Fig. 7; the model includes the measured lab spectra obtained at a resolution of 6 Å (at electron energies of 9, 11, 12, 14, 16, 18, 20, 22, 26, 31, and 100 eV) by Ajello and are similar to those shown in Ajello et al. (2002, Fig. 4). Like Ajello et al., our model distinguishes between MUV 1 (SO₂ + e⁻ → SO($\tilde{A}^3\Pi$) + O(³P) + e⁻) and MUV 2 (SO₂ + e⁻ → SO₂($\tilde{A}^1A_2, \tilde{B}^1B_1, \tilde{a}^3B_1$) + e⁻) excitations and therefore the Ajello et al. spectrum data are divided into two regions: MUV 1 below 2670 Å and MUV 2 above (as shown in Fig. 7). However, note that Ajello et al.'s (2002) spectral data only extends to 4400 Å (for these energies and this resolution) whereas the total MUV 2 emission spectrum extends to 6000 Å. In order for our spectral data to be consistent with the cross section data which is computed using the total emission intensity, it was necessary to extend the lab spectra to 6000 Å. This was accomplished by fitting an exponential curve from 3900 Å to 4400 Å for each of the measured spectra, which was then grafted at 4500 Å to extend the spectrum out to 6000 Å, as seen in Fig. 7b.

It should be noted that the area under the simulated emission spectrum (the intensity per Angstrom) is determined by the number of excitation-emission events which is in turn dependent on the MUV cross sections. This is important because we have laboratory spectral data at relatively few incident electron energies so, for a general

electron energy, we must interpolate between the available spectral data. While the shape of the spectra may be distorted due to interpolation error, the overall emission intensity in that spectral band should not be affected. Also, as the incident electron energy increases, the shape of the MUV 1 spectra changes very little (though the area increases dramatically; e.g., compare the 11 and 12 eV spectra in Fig. 7a) and the shape of MUV 2 spectra changes relatively gradually (Fig. 7b). Therefore simple linear interpolation between the two laboratory spectra at energies bracketing the incident electron energy is used to generate an approximate spectrum from which the emitted photon's wavelength is determined. In other words, for a simulation electron with an energy, E_e , above 9 eV undergoing an MUV interaction, the resultant spectrum, $I(\lambda, E_e)$, is:

$$I(\lambda, E_e) = W * I(\lambda, E_l) + (1 - W) * I(\lambda, E_u), \quad W = \frac{(E_u - E_e)}{(E_u - E_l)} \quad [1]$$

where $I(\lambda, E_u)$ is the lab spectrum with the closest energy, E_u , above the energy of the electron and $I(\lambda, E_l)$ is the nearest lab spectrum with energy E_l lower than E_e . Since the threshold for MUV 2 emission is 5.3 eV and the lowest incident electron energy we have spectral data for is 9 eV, we assume that the MUV 2 emission spectrum does not change significantly for incident electrons below 9 eV. Therefore, all electrons below

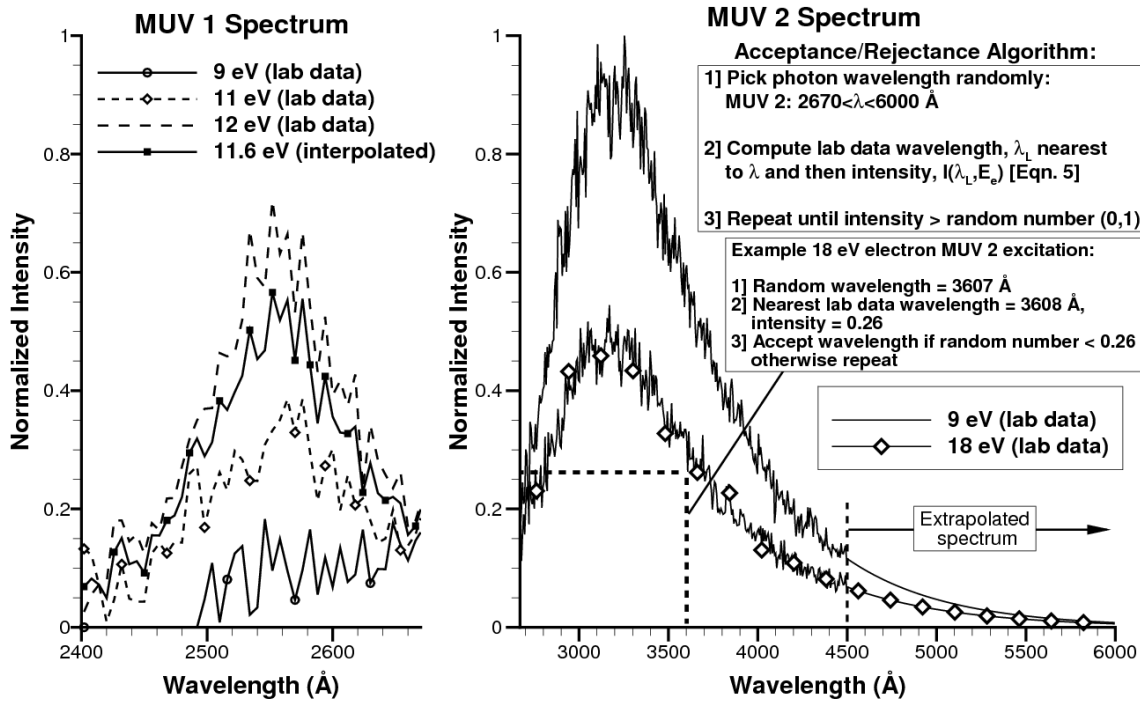


Fig. 7: Representative measured spectra (Ajello et al., 2002) at several incident electron energies for (a) MUV 1 and (b) MUV 2 spectra. In (a) one sees that even below the threshold energy for MUV 1 excitation (10.43 eV) there is emission because the SO₂ quasicontinuum extends to ~ 2500 Å for MUV 2 excitations. Note that the intensity of the 9 eV spectrum below a wavelength of 2492 Å is set to zero because the intensity at lower wavelengths oscillates about zero. Also shown in (a) is the interpolated spectrum (Eq 1) for an MUV 1 excitation occurring due to an 11.6 eV electron. In (b) the exponential curve fit used to extend the MUV 2 spectra to 6000 Å is shown as well as an outline of the acceptance/rejection algorithm for an MUV 2 excitation due to an 18 eV electron. Note that, for computational efficiency, the MUV 1 and MUV 2 spectra have been scaled such that the peak intensity for all electron energies is less than or equal to unity.

9 eV which cause an MUV 2 excitation use the 9 eV spectrum. Similarly, any electrons above 100 eV use the 100 eV spectra (MUV 1 or MUV 2) to generate the emitted photon. All electrons with energies between 9 eV and 100 eV use Eq(1) to generate a spectrum from which the photon wavelength is drawn. For a given MUV excitation event, the wavelength of the emitted photon is chosen via acceptance/rejection on the appropriate spectrum given the incident electron's energy (Fig. 7b). Acceptance/rejection of the photon wavelength for a given excitation event and electron energy is accomplished by picking a random wavelength (within the spectral range for that emission type) and a random number until the intensity of the normalized spectrum at the currently picked wavelength is greater than the current random number.

If an electron-SO₂ MUV interaction occurs, then it is assumed that the excited molecular state always spontaneously decays immediately (no collisional de-excitation, probability of emission for the m^{th} excited particle, $P_{emit,m} = 1$) at the current position of the electron-neutral interaction. This is a reasonable assumption since the Einstein-A coefficients for MUV transitions are large ($\sim 10^5 \text{ s}^{-1}$) compared to the collisional quenching rate ($< 10^2 \text{ s}^{-1}$) and an excited molecule would travel less than $\sim 1 \text{ m}$ during the mean lifetime. If an electron-O($2p^4 \ ^1S$) excitation occurs (emission primarily at 2972 \AA), then the probability that the m^{th} excited O atom will emit rather than be collisionally quenched is

$$P_{emit,m} = A/(\nu_{Q,tot} + A), \quad [2]$$

where the Einstein-A coefficient, A , is equal to $7.54 \times 10^{-2} \text{ s}^{-1}$ for emission from O($2p^4 \ ^1S$) and $\nu_{Q,tot}$ is the total quenching collision rate. The total quenching rate, $\nu_{Q,tot}$, is computed using the species densities and the gas temperature at the position of the excited O atom with an assumed quenching probability of unity. Since the distance a typical excited O would travel during the mean lifetime of the excited state ($\sim 13 \text{ s}$) is small ($\sim 1 \text{ km}$) compared to the atmospheric scale height ($\sim 10 \text{ km}$) and to the resolution element of the simulation's output grid ($\sim 60 \text{ km}$), the motion of the excited oxygen is neglected and emission is counted as occurring at the excitation location. Since each simulated electron (and hence each electron-neutral interaction) represents a large number ($\sim 10^{10}$) of real electrons, Eq(2) is used to scale the individual simulated emission event (as opposed to allowing emission if a random number was less than $P_{emit,m}$) in order to obtain better statistics.

The current model assumes that the atmosphere is optically thin in the MUV spectrum since the SO₂ photoabsorption cross section oscillates between 1×10^{-19} to $1 \times 10^{-18} \text{ cm}^2$ from 2500 \AA and 6000 \AA (Manatt et. al, 1993 and Ahmed et. al, 1992) and the largest line-of-sight column densities are $\sim 10^{17} \text{ cm}^{-2}$ resulting in a maximum optical depth of less than 0.1. Similarly, S₂ absorption through Pele (presumably a

local source of S_2) peaks at 30% at 2750 Å and is less than 10% below 2550 Å and above 3000 Å (Spencer et al. 2000). Also, we assume that no other species has an absorption cross section much larger than SO_2 ($\gg 10^{-18} \text{ cm}^2$) in this wavelength range. Note that the following simulation results will lack any absorption features to the extent that they are present.

4.2 Results

In order to reduce the simulation noise, each case presented here was run multiple (10) times with different random number seeds and the resultant MUV spectra were then ensemble averaged to give the plotted results. When comparing Io's simulated spectrum (computed with a resolution of 6 Å) to the observed spectrum, the simulated spectrum was boxcar smoothed using a resolution element of 108 Å. For the smoothed simulated spectrum, the Monte Carlo noise was less than 2% except near 2220 Å, where there is virtually no emission. In each simulation, the thermal component of the plasma torus was assumed to have an upstream density of 3600 cm^{-3} (Frank et al., 1996). Furthermore, the upstream electron temperature was allowed to vary between 3–10 eV; prior observations have constrained the torus electron temperature at Io's orbit to 4–6 eV (Sittler and Strobel, 1987; Schneider and Trauger, 1995). In addition, a low density, low energy ($\sim 35 \text{ eV}$) non-thermal component of torus electrons could be very important to the MUV emission as opposed to the $\sim \text{keV}$ component, which is expected to not contribute much to the MUV emission intensity (Bhardwaj and Michael 1999). Oliverson et al. (2001) discussed this low energy non-thermal component and its importance for [O I] 6300 Å emission; here we simulate cases with several different densities (non-thermal/thermal densities from 0–7%) for the non-thermal component. Note that the low-energy non-thermal density is roughly constrained to be less than 10% of the thermal density based on short timescale fluctuations where the electron flux varies several percent but the energy flux varies by 30–50% (Oliverson et al., 2001). Furthermore, the non-thermal component's energy distribution was assumed to be a Gaussian centered at a mean energy of 35 eV and with a standard deviation

of 2.5 eV. Note that the simulated intensity is proportional to the upstream thermal density since the excitation rate is proportional to the electron density and the current model uses a precomputed static target atmosphere and fields (which in reality will change with the electron density). The fields in the current model were simulated using the same upstream electron density of 3600 cm^{-3} (Combi et al., 1998). The simulated MUV emission spectrum is shown in Fig. 8 for several upstream thermal electron temperatures assuming Pele and Surt are active and Tvashtar and Dazhbog are inactive. In Fig. 8a the thermal and (1%) non-thermal emission spectra are shown separately. Note that the spectrum for the non-thermal electrons shows relatively little MUV2 emission, but shows significant MUV1 emission that is essentially equivalent to the thermal 3 eV MUV1 intensity. Figure 8a implies that if there is no non-thermal component of torus electrons, then the emission spectra is best fit by an upstream temperature of ~ 10 eV, greater than the otherwise observed ~ 5 eV (Schneider and Bagenal, 2006): In Fig. 8b the spectra are simulated assuming a 5% non-thermal component. In this case the observed spectrum is best fit by a thermal temperature of 5–6 eV; 4 eV thermal electrons are generally too dim and 7 eV thermal electrons result in too much SO emission near 2550 Å (a smaller fraction of non-thermal electrons would correct this though). The 5–6 eV simulations fit the average intensity from 3000 to 3200 Å relatively well and the slope of the emission intensity from 2700 to 3000 Å surprisingly well. It is not clear if the fine-scale features from 2700 to 3000 Å are noise or real (if real they are probably due to S_2 absorption which is not included in the present simulations). Similarly, the large emission feature at 3200 Å ($\sim 20\%$ decreased intensity) might not be real and will be addressed in the discussion section.

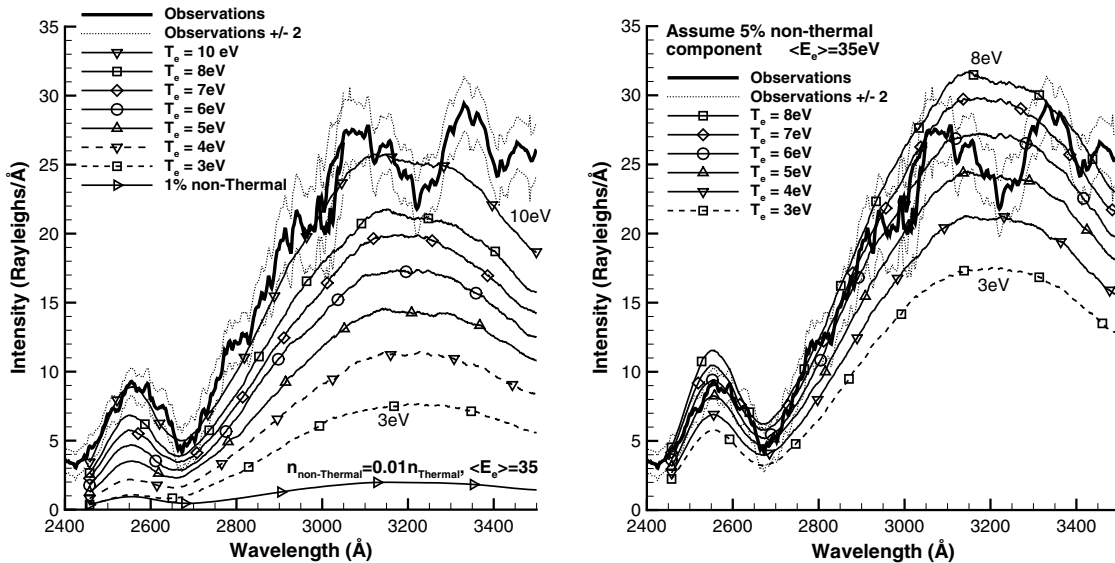


Fig. 8: The observed spectrum (and the $2\text{-}\sigma$ error spectra) from 2400 to 3500 Å (through the larger effective aperture) along with the simulated MUV emission spectrum with Pele and Surt active. In (a) the simulated spectrum is shown for various upstream thermal electron temperatures (3–10 eV) and for a 1% non-thermal component with a mean energy of 35 eV. In (b) the simulated spectrum is shown for a combination of upstream thermal electrons and a 5% non-thermal component.

Our simulation fits are by eye to the entire spectrum at a given upstream thermal temperature and non-thermal density. This means matching the SO emission peaking at ~ 2550 Å, the slope of the SO₂ MUV 2 emission from 2700–3000 Å, and the mean of the local oscillation from 3050–3300 Å, as if SO₂ were the only significant source of emission (and absorption). Additionally, while a more rigorous fitting (e.g. least squares) could have been performed, it would add little given the levels of uncertainty in the non-thermal component and the Pele-type plume activity.

Figure 9 shows the ratio of the peak MUV 2 to peak MUV 1 emission intensity for various upstream thermal electron temperatures and constant non-thermal components. The peak MUV 1 wavelength is taken to be 2550 Å and the peak MUV 2 wavelength is taken to be 3150 Å (this is roughly the location of the lab spectrum’s MUV 2 peak and is outside of the observed intensity dip at ~ 3200 Å). The reason to examine the ratio of the peak intensities and not just the absolute intensities is because the upstream thermal electron density is also variable; comparing the intensity ratio allows us to eliminate the first order effect of the thermal electron density. It is probable

that the density effects one emission peak more than the other (e.g. increased thermal electron density will likely lead to increased SO relative to SO₂ in Io's atmosphere and hence more direct SO excitation), but to first order the thermal electron density increases both peaks' excitation rate linearly.

As shown by the dashed line in Fig. 9, the observed ratio is 2.8 (+0.7, -0.4) with most of the uncertainty arising from the variance in the MUV 2 peak intensity. Given the amount of non-thermal electrons, one can constrain the electron temperature from Fig. 9. Unfortunately the large uncertainty in the observed ratio and the fraction of non-thermal electrons limits the constraint on the upstream electron temperature. In

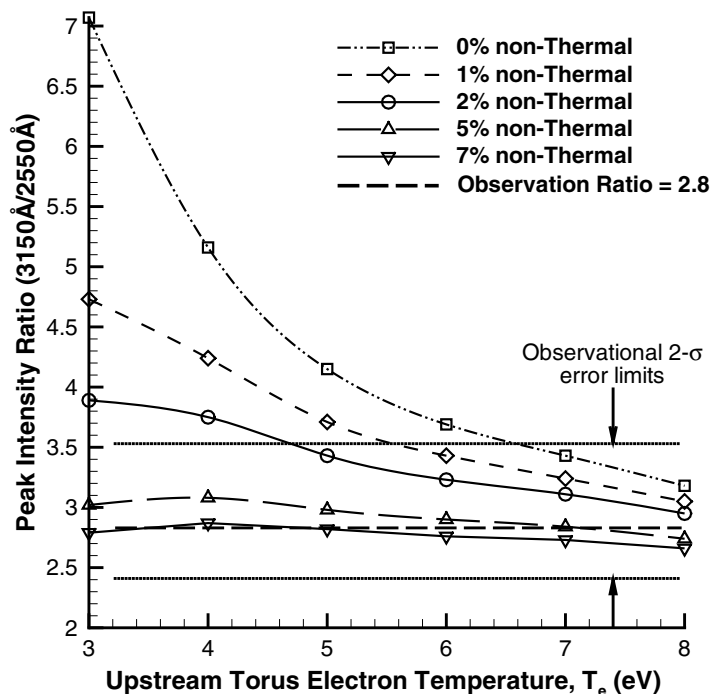


Fig. 9: Ratio of the peak MUV 2 (3150 Å) to peak MUV 1 (2550 Å) emission intensity for various upstream thermal electron temperatures and non-thermal components. Symbols are the simulated ratios (assuming a constant non-thermal component with mean energy of 35 eV) and the observation and its noise constraints are given by dashed and dotted horizontal lines, respectively.

order to reproduce the peak intensity ratio between the two emission peaks without any non-thermal electrons, the upstream electron temperature needs to be ~ 10 eV. At lower thermal temperatures there is insufficient flux of the high energy electrons necessary for MUV 1 emission relative to the flux of the lower energy electrons that excite MUV 2 emission. On the other hand, if there is a 5% non-thermal component then all upstream

thermal electron temperatures fall within the uncertainty limits for the peak intensity ratio, with the 7 eV thermal electron simulation case matching the observed ratio. The peak intensity ratio curves decrease and flatten as the non-thermal component increases because at the 5% level, the non-thermal emission is comparable to the low temperature (3 eV) thermal emission (due to lower energy flux at the energies required for MUV 1 and MUV 2 excitation) and the MUV 2/MUV 1 emission ratio for a 35 eV non-thermal component is ~ 2.1 (see Fig. 8). While obviously not a unique solution given the uncertainties, a good fit for the upstream electron temperature accounting for the peak intensity ratios and the absolute intensities is a thermal temperature of 5–6 eV and a non-thermal density that is 2–7% of the thermal density.

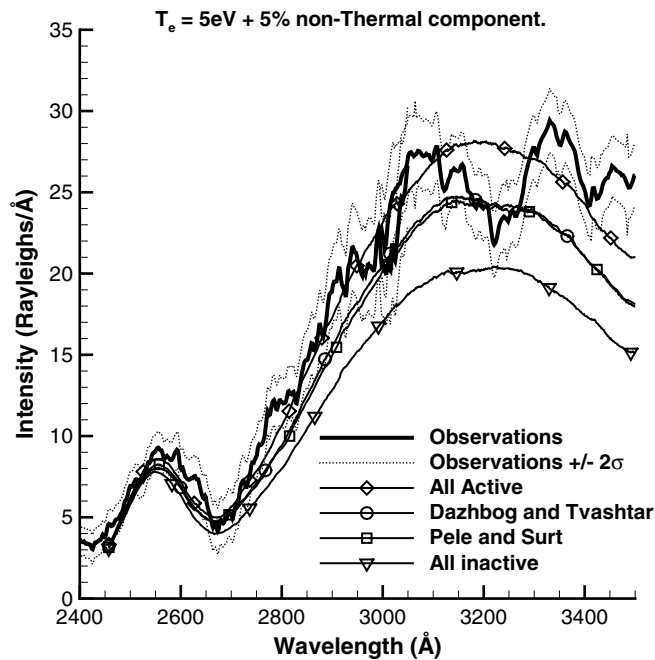


Fig. 10: Sensitivity of the simulated spectrum on Pele-type plume activity (Prometheus-type plume activity held constant) for an upstream electron temperature of 5 eV and a 5% non-thermal component. The plume activity is varied for several cases: Case 1 (Dazhbog, Pele, Surt, and Tvashtar), Case 2 (Pele and Surt), Case 3 (Dazhbog and Tvashtar), and Case 4 (None active). Note that the intensity is insensitive to which plumes are active, but sensitive to the number of active Pele-type plumes.

While there is uncertainty in the non-thermal component, there is also uncertainty in which Pele-type plumes were active at the time of the observation. Assuming that the upstream temperature is 5 eV and the non-thermal density is 5% of the thermal density

based on the results in Figs. 8 and 9, the sensitivity of the simulated spectrum to Pele-type plume activity, several cases were run for each of the various combinations of active Pele-type plumes. Figure 10 shows the cases with all the Pele-type plumes active, just Pele and Surt active, just Tvashtar and Dazhbog active, and all giant Pele-type plumes inactive. While the MUV 2 emission intensity is moderately sensitive to the number of Pele-type plumes that are active, it does not depend strongly on which specific Pele-type plumes are active. This is because, for this viewing geometry, the canopies of the Pele-type plumes are all still visible and most of the added emission due to the Pele-type plumes originates from the canopy region (see line of sight electron energy deposition in Moore et al., 2010a; Fig. 16). Furthermore, the MUV 1 emission intensity was found to be insensitive to even the number of Pele-type plumes, presumably because the electron energy rapidly degrades below the threshold energy required for the MUV 1 excitation. Finally, variation of the smaller, Prometheus-type plumes causes similar, yet smaller changes in the emission spectrum. Unfortunately this means that the specific plume activity cannot be well constrained through examination of the disk-averaged MUV emission spectrum.

5 Discussion

Comparison of the merged CCD or MAMA spectra extracted through the two effective apertures having different sizes in the NE-SW spatial dimension provides an indication of how Io's emission is distributed beyond the disk. The results may not be representative of this direction owing to the rectangular shape of these apertures; however, the intensity is brightest nearest Io, reducing the dependence on aperture geometry. Since the intensity is referenced to Io's solid angle, the difference between these spectra is a measure of the photon flux from the additional rows summed. The difference spectrum is more reliable for the MAMA observations because the zero level for each aperture was set close to the floor at 2200\AA , while the accuracy of the CCD extraction relies entirely on the success of the sky subtraction.

For both eclipse exposures combined, Io's spectrum shows distinctly brighter emission from SO (lower Fig. 2b), SO₂ (upper Fig. 5), and S I (lower Fig. 2b) through the larger effective aperture. The excess is up to 1–2 R/Å for the MAMA spectra (i.e. about 21% for S I and 11–14% at longer wavelengths vs. the 32% aperture difference). For the brighter CCD spectra, the excess is 3–7 R/Å (or 10–13% vs. the 50% aperture difference). This result indicates that SO₂, SO and S I emission all extend beyond the diameter of Io's disk, consistent with plasma torus electron bombardment and the dissociative excitation of Io's SO₂ atmosphere. The percentage increase is greatest for S I, suggesting that it is the most extended, which would be consistent with its having the largest scale height due to its lowest nuclear weight, and with previous HST observations of S I. The unidentified emission also appears to be well extended, by this metric. However, any gradient of S I, SO, and SO₂ emission across Io's disk is not clearly discernible from the MAMA spectra because of the fairly good agreement between the halves for especially the SO and SO₂ emission (after offsetting the spectra to zero out the dip at 2200 Å). The quality of the agreement is good enough (Fig. 2a, upper Fig. 2b) that there cannot be a pronounced NE-SW asymmetry in their emission, which is qualitatively consistent with the limited asymmetry found for the SO₂ profile in lower Fig. 5). On the other hand, lower Fig. 5 and upper Fig. 1b both imply a pronounced asymmetry in the NE-SW direction for the unidentified emission, brighter than the SO₂ on the NE side, which might indicate an association with the wake emission.

Io's high magnetic latitude during the CCD observations (+9° to +8°; Table 1) implies brighter emission along the southern limb and a displacement of Io's wake to a southern latitude. With an active Pele, this configuration would favor brighter emission in Io's SW half. However, emission from the wake and Tvashtar would favor the observed brighter NE half since Tvashtar lies at high latitude and was at +142° longitude relative to Io's sub-Earth point at the time of the CCD eclipse observations. An active Tvashtar plume would have been peaking over the NE limb, with visibility

improving throughout eclipse. So Tvashtar may have been active instead of Pele at the time of these observations (Moore et al. 2010b) and been a significant source of the unidentified emitter while contributing comparatively less to the overall SO₂ emission due to the presence of the sublimation atmosphere

One might question whether Io's observed spectrum might simply be explained by a solar component having highly magnified, originally weak, absorption features arising from the nearly tangential path of sunlight refracted through Jupiter's atmosphere. We are confident a solar component is not included in the extracted spectra for several reasons: The brightening of Io in Jupiter's shadow approaching umbral egress suggests that sunlight refracted into Jupiter shadow significantly illuminates Io only within 13 min of the penumbra (Geissler et al. 2004). Since the first CCD exposure did not begin until 13 min into the umbra, there should be negligible solar contribution to the CCD spectra. This time interval depends somewhat on Jupiter's subsolar latitude, which causes Io's path to lie along an umbral chord. However, Jupiter's tilt at the time of the Geissler et al. (2004) eclipse B and C observations was 3.31°, close to the 3.26° tilt for the HST observations reported here, so the 13 min limit should apply. Formisano et al. (2003) discussed Io's methane continuum spectrum in eclipse, arising from sunlight refracted tangentially through Jupiter's atmosphere into shadow. Their results, however, indicate that such magnification is not possible at visual wavelengths, at least without great extinction of the solar continuum at Io. Of the 4 strong absorption-like features shown in upper Fig. 5, only the middle two (4870 & 5120 Å) lie close to strong CH₄ band wavelengths at 4850 and 5100 Å, reported in the spectra of Uranus and Neptune by Karkoschka (1998; Fig. 1). However, their relative strength differs greatly and there is no trace of Io's 4250 Å feature in his spectra.

Additionally, the rising slope of Io's CCD spectrum above 4000 Å is unlikely to be of solar origin. This is because Galileo and Cassini images taken during Io eclipse show emission in this wavelength range that has brightness comparable to our integrated spectra: Galileo found that Io's eclipsed dayside (Jupiter facing) emission intensity

(observed over 350W-70W) through the GRN filter (5100–6050 Å) was 40% that of its nightside (anti-jovian) emission intensity (observed during eclipse over 70W-160W); i.e., 8.0 vs. 20 kR, respectively (Geissler et al. 1999). If the emission were uniform over this bandpass, these would correspond to 8.4 and 21 R/Å. The eclipsed dayside value of 8.4 R/Å is dimmer than the value of ~ 30 R/Å observed in our CCD spectrum, but the GRN filter extends beyond our 5700 Å limit. For Io's nightside, Cassini found 102 ± 8 kR through the BL1 filter (3900–5000 Å) (Geissler et al. 2004). This corresponds to a mean of 93 R/Å. Multiplying by Galileo's 40% ratio (assuming it still applies during the Cassini time frame), we estimate the eclipsed dayside to be 37 R/Å. Our value then lies between the two spacecraft values, making it plausible. Finally, differential refraction of sunlight by Jupiter's atmosphere would cause the half of Io deeper into early eclipse to be illuminated by more dispersed, and therefore dimmer, sunlight. However, the spectrum above 4500 Å on Io's NE side, which is closer to Jupiter and so deeper into eclipse, is brighter, not dimmer (Fig. 1b). This is further evidence that solar illumination is not significant. We conclude that the unidentified band between 4100–5700 Å is practically entirely Iogenic emission.

Cassini/ISS camera observations through the clear filter (0.24 - 1.1 μm) indicate that Io's disk-averaged spectrum dropped by a factor of 2 during the first 18 min of umbral eclipse and then changed very gradually, presumably due to the changing aspect of volcanic plumes and surface emission (Geissler et al. 2004). As mentioned above, these observations indicated that illumination of Io by sunlight refracted or scattered into Jupiter's shadow was negligible after 13 min into eclipse, so the CCD spectra do not have a solar component. However, the first MAMA exposure began only 1 min after umbral ingress (Table 1), while still illuminated by refracted sunlight. Nonetheless, owing to Io's low MUV 1 albedo and the falloff the solar flux with wavelength, Io's diffusely reflected solar spectrum during umbral eclipse from all sources was negligible relative to Io's emission at wavelengths below 3100 Å, and was at most very weak up to 4000 Å. This is illustrated in Fig. 4 by Io's dashed daytime continuum spectrum

that has been normalized to fit Io's observed eclipse spectrum at 5700 Å. Even if the observed intensity at 5700 Å were entirely sunlight diffusely reflected by Io after refraction in Jupiter's atmosphere, the spectrum observed below 4000 Å must primarily be Iogenic emission and the MAMA spectrum reveals no solar continuum component. Note that the effect of extinction and refraction of sunlight in Jupiter's atmosphere only steepens this slope relative to Io's emission spectrum, further reducing Io's solar contribution at MUV wavelengths.

Finally, the direct enhancement of Io's emission at any wavelength by refracted sunlight via photoelectron generation and impact is unlikely since Rayleigh scattering and absorption in Jupiter's atmosphere would have greatly attenuated the NUV-FUV ionizing wavelengths incident on Io. Nevertheless, the eclipse-resolved MAMA spectra, which are adjusted to fit the combined CCD spectrum over 3000–3100 Å, appear weaker later in eclipse below 2900 Å (Fig. 2a), which includes the SO feature at 2550 Å and the S I multiplets. Noise may contribute to the difference between these spectra, but the agreement between the two halves for each eclipse phase suggests that the temporal change is real.

The emission from SO₂ and its dissociative products is brighter in daylight owing to direct photon excitation and the impact of photoelectrons generated by solar EUV radiation. After eclipse ingress, the solar contribution, including fluorescence, relaxes as residual photoelectrons are lost to the sweeping magnetic field or become spent energetically so that they can no longer excite; and as emitting species recombine. For conservative estimates of the plasma flow speed around Io (e.g. Saur et al. 2002), most residual photoelectrons are convected past Io by the Jovian magnetic field in less than 10 min. Moreover, the collision time scale for energy-losing electron collisions is shorter than 10 min, especially deep in the atmosphere where the electrons convect most slowly past Io. Here, the collision time scale is of O(0.1 s). Therefore, while some photoelectrons may remain after 10 min, they will very probably not be energetic enough to explain the falloff off the eclipse light curve observed by Cassini continuing

beyond 10 min. The emission is then maintained at a lower rate by the torus electrons. Potential MUV 1 intensity loss mechanisms are plasma impact dissociation of SO and SO₂, recombination of SO+O, photoelectron loss, and partial atmospheric freezeout.

However, the plasma dissociation lifetimes of SO, SO₂, and O₂ are comparable to the ~2 hr duration of the eclipse (Moore et al. 2009), typically much shorter than the SO+O recombination time, which is far too slow to explain any weakening in the MUV 1 emission. The photo-dissociated component of these species will persist well into eclipse if not condensable. The concentration of photo-dissociated condensables like S and O will become less as the eclipse progresses since they will diffuse slowly to the surface and become lost. Plasma dissociation might decrease the excess solar-generated SO column by ~20% over the first 30 min of eclipse; during which time the total SO₂ column could drop by an order of magnitude due to condensation onto the surface, if SO is condensable (Case 2, Fig. 8, Moore et al. 2009) as expected based on analysis by Baklouti (2008). It is thus reasonable to neglect both recombination and the plasma dissociation contributions to the weakening of the MAMA spectrum.

Therefore, since Io's illumination by sunlight refracted into shadow by Jupiter's atmosphere was very weak at the MAMA wavelengths, the drop in the emission intensity between these exposures indicates partial atmospheric collapse and the loss of energetic photoelectrons capable of exciting the MUV 1 emission. The continuing falloff of the eclipse light curve observed by Cassini between 13 min and the floor at 18 min (Geissler et al. 2004) is evidence that the falloff after ~10 min is driven primarily by the progressive freezing out of Io's atmosphere rather than by the attenuation of photoelectrons. The combined spectrum, Fig. 2b, thus likely represents a less than asymptotically collapsed sublimation atmosphere. In order to know which effect dominates early in eclipse, a more complete model that accounts for the time varying atmosphere and electron energy distribution would be needed. After the first 10 min or so, the plasma dissociation contribution is likely negligible.

Comparison of the two eclipse-resolved CCD spectra (Fig. 1b lower) around the

SO₂ emission peak near 3150 Å provides no obvious indication of ongoing atmospheric collapse. This is largely because the CCD observations did not begin until 13 min into the umbra (3.7 Io diameters), just as the illumination by sunlight refracted in Jupiter's atmosphere became negligible. Hence, neither sunlight refracted by Jupiter nor photoelectrons affected the CCD spectra. Atmospheric collapse would have been the dominant emission loss process for these observations.

According to the Cassini clear-filter eclipse light curve, at the start of the first CCD exposure, the disk intensity had dropped by 73% of its range, which is limited by emission from the volcanic plumes (Geissler et al. 2004) or by non-condensables preventing further rapid collapse (Moore et al. 2009). The intensity and atmospheric column should have dropped the remaining 27% during the first ~3 min of the 12 min exposure as Io penetrated 5.1 Io diameters into the umbra, where the eclipse curve levels off. However, change in the emission intensity from atmospheric collapse would be less apparent in the MUV 2 spectrum than for the MUV 1 spectrum because Io's S₂ emission practically superposes the MUV 2 spectrum, and it arises almost entirely from volcanic plumes, which are unaffected by eclipse (Geissler et al. 2004, Moore et al. 2010b). Since the second CCD exposure was taken during the flattened section of Io's eclipse curve, little additional freezeout should have occurred during it. Given the constant S₂ emission, the near agreement between the two spectra would be consistent with limited atmospheric collapse occurring during the first exposure, perhaps indicative of the final 27% drop in light occurring during its first quarter.

The SO₂ MUV 2 electron impact spectrum peaks near 3150 Å and drops 50% by 3570 Å (Fig. 5 upper; Ajello et al. 2002) where the reflected solar continuum is still weak (Fig. 4). An emission source on Io is needed from ~3300 to 5700 Å to fill the void left between Io's observed eclipse spectrum and the declining SO₂ emission tail. This was recognized by Geissler et al. (2004) on the basis of narrow-band Cassini ISS images of Io in eclipse, which indicated that there must be an additional source of emission in Io's visual spectrum because fitting the modeled SO₂ spectrum to the

observed intensity resulted in an emission shortfall there. They suggested that this source is S_2 , which has been detected in Pele type plumes (Spencer et al. 2000). However, laboratory spectra of S_2 in this wavelength range have been lacking and this suggestion could not be tested. The unidentified emission band reported here accounts for the emission between 4100 Å and the end of the spectrum at 5700 Å; however, that still leaves a deficit between the observed and simulated spectra between ~ 3300 Å and 4100 Å. While this might be filled by S_2 emission, an alternative explanation for the deficit may be that the unidentified species is responsible for all the excess emission observed above ~ 3300 Å.

Io's broad emission peak centered at 3150 Å does exhibit structure that appears to be statistically significant. A dip is apparent at 3200 Å bounded by two local peaks at 3050 Å and 3350 Å (Figs. 4 & 8 for the smaller and larger extracted apertures, respectively). Simulations done by Moore et al. (2010b) using theoretical S_2 electron impact spectra do not show a peak at 3350 Å. However, the S_2 electron impact emission spectrum, and to a lesser extent, the excitation cross sections are uncertain; laboratory electron impact spectra are needed for S_2 at relevant electron energies from ~ 3300 Å to ~ 4100 Å to resolve this issue definitively. Gaseous S_2 absorption in plumes (Spencer et al. 2000; Jessup et al. 2007) should be negligible at the 3200 Å dip and SO_2 self-absorption might absorb up to 5%, not enough to explain the dip.

Having established the reality of Io's emission in the CCD spectrum above 4100 Å, as opposed to the spectrum being noise or diffusely reflected sunlight transmitted by Jupiter, we now rule out the lowermost spectrum in Fig. 4 that shows the result of subtracting 0.7% more sky than the nominal amount. This is justified because this spectrum would result in excessive negative emission (at resolution element 31 Å) than allowed by the propagated error. In addition, the uppermost spectrum of this Figure is unlikely primarily because it is inconsistent with the low eclipse intensity measured in the Galileo GRN image discussed above.

The regularity of the features in Fig. 1e suggests a molecular band spectrum and

the spacing suggests a vibronic band, having both vibrational and electronic excitation. In vibronic bands the vibrational selection rule $\Delta v=1$ no longer holds. The transition sequence number “s” in Fig. 1e is related to the vibrational quantum number “v” through a discrete linear transformation: $v = \pm s + \text{integer}$. The continuity in line spacing, if not in intensity, across $s=13$ suggests a single progression where the intensity varies widely according to the overlap between successive initial or final vibrational wave functions of the different electronic states. The linearity suggests a deep well for the intra-molecular potential with little centrifugal stretching. The linearity and spectral region also is characteristic of bending modes of vibration, which would require at least 3 atoms in the source molecule. SO_2 and S_2O are therefore potential candidates. The only candidate molecules listed in the GEISA and HITRAN databases with lines in this spectral range are OH and H_2O . The OH lines are listed only below $19,020 \text{ cm}^{-1}$ while 6 prominent H_2O bands span this spectral interval below $23,000 \text{ cm}^{-1}$. Since both disagree with the unidentified spectrum, OH and H_2O can be ruled out. Other potential candidate gases might include the positive or negative ions of S, O, SO, S_2 , O_2 , and SO_2 . The first negative band structure of O_2^+ lies in the observed range, and is supported by our plasma simulations, but appears to be ruled out because it does not agree with the laboratory spectrum shown in Pearce and Gaydon (1976).

Our results show that SO_2 MUV 1 and MUV 2 excitation are, at least, important sources of emission from 2400 \AA to 3400 \AA . Additional emitting species would reduce SO_2 's overall importance to the emission intensity in this region as compared to the simulations presented here. Any additional emitter would tend to increase the simulated intensity because the electron energy flux is currently not completely absorbed as the flux tube crosses Io; however, with the addition of a sufficiently strong emitter that limit may be reached. Another emitting species might explain some of the discrepancies between our simulated spectrum and the observations, e.g. the peaks located at 3150 \AA and 3350 \AA . SO_2 is the dominant gas in Io's atmosphere and plumes, so a minor or trace species would have to have a much larger excitation cross section than SO_2 in

order to make a significant ($>10\%$) impact on the emission intensity. Prior simulations that include S_2 and use a theoretical excitation cross section ~ 30 times larger than the SO_2 MUV 2 excitation cross section found that the simulated intensity near 3100 \AA increased by only $\sim 40\%$ (Moore et al., 2010b). Finally, if only S_2 or another species that emits above 3000 \AA were added, the ratio of the peak intensities shown in Fig. 9 would change, likely leading to a different best-fit upstream non-thermal electron density or even a different upstream thermal temperature.

6 Conclusions

Emission has been detected during eclipse in the SO_2 MUV 2 wavelength range with a peak near 3150 \AA (of $26 \pm 2 \text{ R/\AA}$ and $29 \pm 2 \text{ R/\AA}$ for the smaller and larger effective apertures, respectively) along with local emission features due to neutral SO_2 daughter species, SO (2550 \AA) and $S \text{ I}$ (1800 \AA & 1900 \AA). Simulation of the SO_2 and SO emission assuming only a contribution from SO_2 excitation and dissociative excitation was able to reasonably match the observed intensity spectrum given the uncertainties, suggesting that dissociative excitation of SO_2 is a significant source of emission by the SO_2 daughter species. Our investigation has led to the following conclusions:

1. The diffusely reflected solar spectrum is expected to be completely negligible in the MAMA eclipse spectra relative to Io's emission owing to extinction of NUV sunlight by Jupiter's atmosphere and Io's low NUV albedo below 4000 \AA . Thus, the MAMA spectra are entirely iogenic emission.
2. The diffusely reflected solar spectrum is not detectable in the CCD spectra because of the late start of the CCD eclipse exposures, after illumination by refracted sunlight became negligible (Geissler et al. 2004). Thus, the CCD spectra are also entirely iogenic emission.
3. Weakening $S \text{ I}$, SO , and SO_2 emission intensity between the eclipse-resolved MAMA spectra (Fig. 2a) indicate ongoing atmospheric collapse due to freezeout and

the decay of residual photoelectrons during the first exposure. This is consistent with the early umbral eclipse phase observed for this exposure when the atmosphere should have not fully collapsed. Due to the extinction of FUV-EUV sunlight in Jupiter's atmosphere, refracted sunlight is unlikely to have excited noticeable emission from Io at any wavelength during umbral eclipse via photoelectron impact.

4. The SO₂ emission for the CCD eclipse observations shows no clear evidence of ongoing atmospheric collapse due to freezeout. This is consistent with the Cassini observations of Io's eclipse light curve (Geissler et al. 2004), which indicate that these observations should have mostly been on the flat plateau of the eclipse light curve.

5. An emission source is needed from ~ 3300 to 5700 Å on Io to fill in the void left by the declining SO₂ emission tail to explain Io's observed spectrum. Because there can be no solar contribution to the CCD spectra, we conclude that the unidentified band found between 4100 – 5700 Å is iogenic emission, indicating the presence of another atmospheric gas species, or a newly observed mode of excitation.

6. Io's SO₂ emission was distributed nearly symmetrically across Io's disk along the NE-SW direction, suggesting a nearly symmetric background atmosphere irrespective of localized volcanic plume activity. In contrast, the unidentified emission was distributed asymmetrically across Io's disk along this direction, being brighter on the NE side and limb, and so may be associated with the wake spot emission or with greater NE volcanic efflux of the unidentified species.

7. The regularity of the features in the spectrum from 4100 – 5700 Å and the average line spacing of 404.5 cm⁻¹ excludes a rotational progression and indicates a vibronic molecular band, having both vibrational and electronic excitation. The linearity of the line spacing and the wavelength regime indicates little centrifugal stretching, which suggests a deep intra-molecular potential well, and suggests excitation of a bending mode of vibration that would indicate a tri-atomic molecule. OH and H₂O are specifically excluded because their database wavelengths do not match the observed spectrum. Potential candidate gases include the positive or negative ions of S, O, SO, S₂, O₂, SO₂

and S_2O ; however, O_2^+ appears to be excluded.

The following conclusions relate to the simulation of these spectra:

8. The MUV 2 emission intensity does not depend strongly on which of the Pele-type plumes are active because the canopies of the Pele-type plumes are all visible for the observation geometry.

9. The MUV 1 emission intensity was found to be insensitive to even the number of Pele-type plumes, presumably because the electron energy rapidly degrades below the threshold energy required for the MUV 1 excitation. Unfortunately this means that the specific plume activity cannot be well constrained through examination of the disk-averaged MUV emission spectrum.

10. Unfortunately the large uncertainty in the observed intensity ratio between MUV 1 and MUV 2 peaks and the fraction of non-thermal electrons limits the constraint on the upstream electron temperature. Without any non-thermal electrons, the best fit upstream electron temperature is 10 eV; however, prior observations of Io's plasma torus have found an upstream thermal electron temperature of 4-6 eV near Io's orbit (Sittler and Strobel, 1987; Schneider and Trauger, 1995; Schneider and Bagenal, 2006). The best fit upstream electron temperature accounting for the peak intensity ratios and the absolute intensities is a thermal temperature of 5-6 eV and a non-thermal density that is 2-7% of the thermal density, which is within the limits suggested by Oliverson et al., 2001. For a 5% non-thermal component, a 5 eV thermal component produces good agreement with the observation from 2400 to 3100 Å.

Electron impact laboratory spectra are needed at relevant electron energies for S_2 from ~ 3300 Å to ~ 4100 Å for an attempt to rectify the discrepancy between the observed and simulated spectrum over this range. Such spectra may also be useful for investigating the structure observed near the broad emission peak of SO_2 in Io's eclipse spectra if extended down to 3000 Å. The FUV laboratory study of the impact spectrum of SO_2 by Palle et al. (2004) is limited to lines below 1700 Å and the finely energy-stepped data of Ajello et al. (2004) is limited to above 2400 Å. Further

laboratory electron impact spectra between 1700–2400 Å would be useful for analysis of the identified (and possibly other) excited sulfur lines, which are only approximately described by existing data. Finally, laboratory investigations are also needed to help identify Io’s unknown emission between 4100–5700 Å.

A more detailed analysis of the spatial variation of the emission over Io’s disk in terms of plasma transport and volcanic activity will be presented in a forthcoming paper.

Acknowledgements

We thank Joe Ajello for providing laboratory data in advance of publication and for helpful comments. We also acknowledge useful comments from Paul Feldman, Gilda Ballester, and Kandis Lea Jessup. We also thank two anonymous referees for their helpful detailed comments and corrections. Support for programs #HST-GO-08169.09-A and #HST-AR-10322.01-A was provided by NASA through a grant from the Space Telescope Science Institute, which is operated by the Association of Universities for Research in Astronomy, Inc., under NASA contract NAS 5-26555. Continuing support was also provided by NASA/OPR grant NNX08AQ49G and NASA grant NNX09AV10G.

Appendix

Effective Apertures: Comparing spectra on opposite halves of Io provides a validation of features in Io's spectrum in the presence of noise. Moreover, differencing the extracted spectra for two effective apertures provides an estimate of Io's extended emission. The 1201x1201 reduced spectral images of the 1024x1024 CCD and MAMA detector arrays both used the same $2.''035 \times 2.''012$ aperture, which was sampled by $0.''051$ and $0.''025$ pixels, respectively. We number the rows of the reduced spectrum spanning the aperture beginning with row 0 near the bottom (NE end), which corresponds to data row 583 and 556 for the respective detectors. Of the approximately 40 CCD rows spanning the aperture, we used the 37 least vignetted rows. Acquisition images showed that Io appeared to be almost centered in the aperture, displaced a few rows towards the NE. Seven rows were averaged on each side of Io ($0.''35$ wide) to extract the sky background (the shaded CCD areas in Fig. A1). To extract Io's spectrum, the sky was interpolated linearly between the approximate mid points of the shaded strips, using the strip averages. The extent of the STIS aperture in the spatial dimension used to extract spectra of Io's disk halves and of Io's disk plus extended emission is also shown in Fig. A1. The extraction aperture for comparing Io's half-disk spectra was the 22 rows centered on Io, yielding an effective aperture of $2.''03 \times 1.''12$ vs Io's diameter of 21 pixels ($1.''08$). The extraction aperture for Io's extended whole-disk CCD spectrum was the encompassing 31 rows shown in the Figure, which resulted in an effective aperture of $2.''03 \times 1.''58$. This is 41% larger than the extraction aperture for comparing the Io halves.

For the MAMA detector, the STIS aperture spanned almost 82 spectral rows; i.e., image rows 556 - 637. Summing the spectral columns of the MAMA spectral image indicated that Io was off center by several rows towards the NE (Fig. A1). The sky average thus included three vignetted rows at the lower edge to improve the S/N of the reference sky background spectrum on this side of Io. Aperture rows 2–16 (image rows 558–572) were averaged after discarding two excessively noisy image rows, 564

and 565, which exaggerated a non-physical, negative dip at 2200 Å). The average was corrected for vignetting by normalizing it to the average of 11 nearby overlapping unvignetted rows. On the SW side of Io, 10 unvignetted rows, 626 to 635, were averaged to form the reference sky spectrum there. The full extraction area was taken to be 61 intervening unvignetted rows, 10 to 70 (image rows 566 to 626), that form an effective aperture of $2.''03 \times 1.''51$. Overlap of the sky spectrum with Io's extended spectrum is neglected in the sky averages. The effect is to underestimate the more extended emission. For summing over Io halves, the effective aperture extended over 46 rows (14–59), corresponding to an area $2.''03 \times 1.''14$ vs Io's diameter of 45 pixels ($1.''12$). The full extraction aperture was 32% bigger than for the extracted halves, all in the spatial dimension.

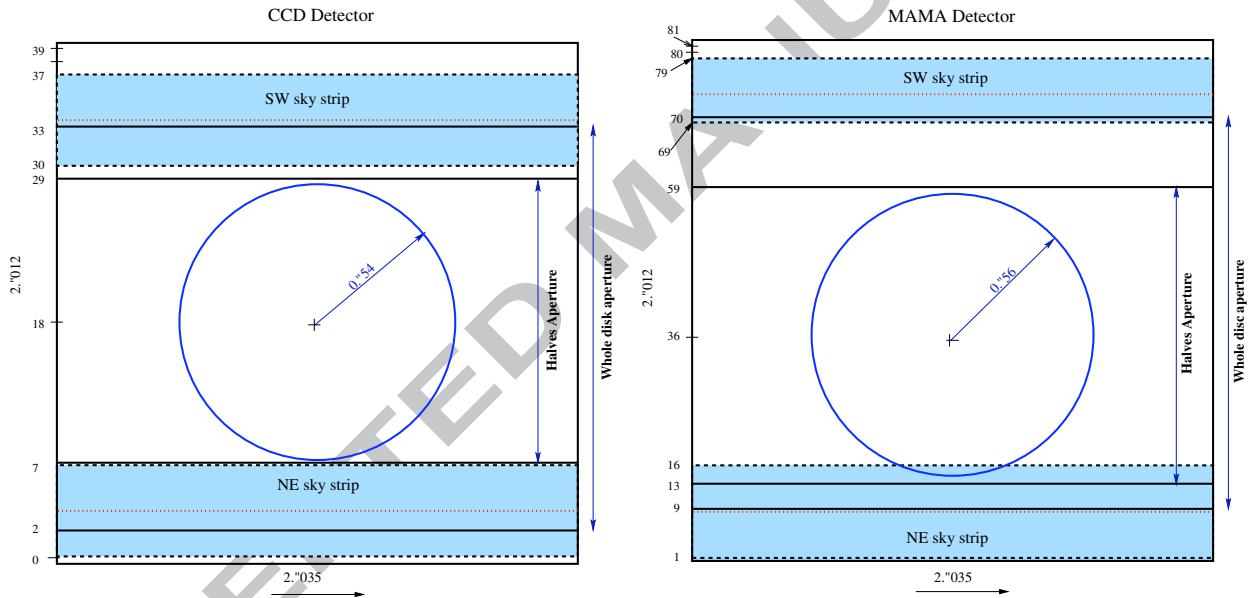


Fig. A1: Aperture layout for the CCD and MAMA detectors. The circle represents Io's disk. The dispersion axis is horizontal and the spatial axis is vertical (NE down; SW up). The ordinate is the detector row number. The extent of the apertures in the spatial dimension used to extract Io's disk halves and to extract Io's disk plus extended emission is indicated. The rows used to extract the average sky background on each side of Io are shaded, and bounded by dotted lines. To extract Io's spectrum, the sky was interpolated linearly between the approximate mid points of the shaded strips (indicated by the dotted lines), using the strip averages.

Whole vs. half disk extractions: For the case of Io's "half-disk" extractions, we estimated which detector row passed through Io's center by first building up the S/N ratio by collapsing the spectral image in the dispersion dimension via summing

pixels along rows. The spectral range summed was limited in order to avoid noisy data at the ends. Experimentation with several wavelength ranges indicated negligible effect on the selected central row. Then we summed the pixels in a fixed number of adjacent rows of the detector corresponding to Io's apparent diameter ($1.''1$). Twenty two rows of Io were extracted for the CCD and 46 rows for the MAMA detector. This process was repeated after shifting the window spatially by one row at a time until the window had scanned Io. The window tallying the greatest count was selected as the one centered on Io; and its central row was adopted as the bisector of Io's disk. The respective extracted central rows were row 18.5 and row 36.5. We note that these rows are canted clockwise with respect to the Jupiter-Io direction by 46° and 28° for observations obtained with the CCD and MAMA detectors, respectively. Because this method is sensitive to the position of Io's limbs, it is less apt to peak on Io's centroid than on Io's center. However, it still may miss the precise center depending on how the emission is distributed, particularly beyond the limb. Nonetheless, such error is acceptable for verifying the reality of Io's spectral features because it still permits a close comparison of the "halves", as shown in the Figures.

a) The independent half-disk spectral extractions: The primary purpose of extracting and comparing independent half-disk spectra was to determine which features seen in the whole-disk spectrum are real. Independently extracted half-disk spectra were obtained by first separately summing the rows of the corresponding effective aperture on either side of Io's mid point and subtracting only the corresponding sky strip on the same side of Io. Because of the gradient in Jupiter's scattered light across the aperture, each sky strip had to be oppositely scaled by a few percent before subtraction to yield approximately balanced but still independent extracted halves. Balancing was achieved by making small opposing adjustments in the normalization of the sky strips to maximize agreement between the extracted halves without appreciably affecting the extracted sum. This permitted close comparison of Io's halves to help validate spectral features. However, balancing forces symmetry on the halves which

would not be appropriate if there is an emission intensity gradient across Io's disk. The extracted zero level is thus not well constrained and may be artificial. Moreover, using only half the available sky background, the independent half-disk extractions are noisier than if all the sky spectra were utilized. They were therefore performed only to establish the reality of features in the CCD spectra.

b) The dependent half-disk spectral extractions: Having established which CCD features are real, the S/N ratio was improved by extracting dependent half-disk spectra for which the subtracted sky background spectrum, observed on both sides of Io, was linearly interpolated spatially at each row across Io's disk and extended emission. This is similar to the whole disk extractions in which all the rows of the larger effective aperture were extracted using a linearly interpolated sky spectrum.

Besides correcting the vignetting, the scaling of the sky strips for this case was adjusted to better cancel the sky in Io's extracted spectrum while avoiding excessive lopsidedness of the extracted spatial emission profile. These scale factors were also adopted for the whole-disk dependent CCD extractions. Balancing was done only in cases where the emission gradient across Io's disk was not of interest: The separate eclipse-combined CCD halves required adjustment to the sky strips less than $\pm 0.9\%$ on either side of Io and the eclipse-combined MAMA halves required $\pm 1.8\%$. Since the eclipse-combined whole-disk spectrum is unaffected by such balancing, balancing was omitted for all *ab initio* whole-disk extractions. Finally, the extracted 1-D spectra were all smoothed to improve the S/N ratio.

The whole-disk extractions of the MAMA spectra were handled as for the direct and alternative whole-disk CCD cases above. However, performing independent half-Io extractions, as done for the CCD observations, gave significantly worse agreement for the MAMA data due to the greater noise. So all the half-disk MAMA spectra were extracted dependently by linearly interpolating the sky spectrum between the sky strips at the approximate centroid points of each Io half-disk. This resulted in two linearly dependent sky spectra that were weighted averages of the sky strips with

weights 0.375 and 0.625 (and vice versa for the other half), which are proportional to the fractional distance of these two symmetric points on Io's disk from the opposite sky strip centerline. Subtracting each interpolated sky strip from its corresponding extracted 1-D half-Io plus sky spectrum yielded the extracted Io-half spectrum. The rescaling of the sky strips was sometimes also constrained to balance the two half-Io spectra better to facilitate a closer comparison. While an artifact in the sky spectrum on one side of Io could affect the extracted dependent spectra of both Io halves, an overall agreement between the halves of broader features should still support their reality.

ACCEPTED MANUSCRIPT

7 References Cited

Allen, C. W. 1976. *Astrophysical Quantities*, Athlone (3rd edition), London.

Ahmed, S.M., Kumar V. 1992. Quantitative photoabsorption and fluorescence spectroscopy of SO₂ at 188–231 and 278.7–320 nm. *J. Quant. Spectrosc. Radiat. Transfer* 47, 359–373.

Ajello, J. M., James, G. K., Kanik, I., Franklin, B. O. 1992a. The complete UV spectrum of SO₂ by electron impact 1. The vacuum ultraviolet spectrum. *J. Geophys. Res.* 97, 10,473–10,500.

Ajello, J. M., James, G. K., Kanik, I. 1992b. The complete UV spectrum of SO₂ by electron impact 2. The middle ultraviolet spectrum, *J. Geophys. Res.* 97, 10,501–10,512.

Ajello, J. M., Hansen, D. L., Beegle, L. W., Terrell, C. A., Kanik, I., James, G. K., Makarov, O. P. 2002. Middle-ultraviolet and visible spectrum of SO₂ by electron impact. *J. Geophys. Res. (Space Physics)* 107, SIA 2-1.

Bagenal, F. 1999. HST-Galileo Io Campaign, *Bull. Amer. Astron. Soc.* 31, 1164–1165.

Baklouti, D., Schmitt, B., and Brissaud, O., 2008. S₂O, polysulfuroxide and sulfur polymer on Io's surface? *Icarus* 194, 647-659.

Ballester, G. E., McGrath, M. A., Strobel, D. F., Zhu, X., Feldman, P. D., Moos, H. W. 1994. Detection of the SO₂ atmosphere on Io with the Hubble Space Telescope, *Icarus* 111, 2–17.

Bhardwaj, A., Michael, M. 1999. On the excitation of Io's atmosphere by the photoelectrons: Application of the analytical yield spectral model of SO₂. *Geophys. Res. Lett.* 26, 393–396.

Combi, M. R., Kabin, K., Gombosi, T. I., DeZeeuw, D. L. 1998. Io's plasma environment during the Galileo flyby: Global three-dimensional MHD modeling with adaptive mesh refinement. *J. Geophys. Res.* 103. 9,071–9,081.

Clarke, J. T., Ajello, J., Luhmann, J., Schneider, N., Kanik, I. 1994. Hubble Space Telescope UV spectral observations of Io passing into eclipse. *J. Geophys. Res.* 99, 8387–8402.

de Pater, I.; Marchis, F., Macintosh, B. A., Roe, H. G., Le Mignant, D., Graham, J. R., Davies, A. G. 2004. Keck AO observations of Io in and out of eclipse, *Icarus* 169, 250–263.

Doute, S., Schmitt, B., Lopes-Gautier, R., Carlson, R., Soderblom, L., Shirley, J., The Galileo NIMS Team. 2001. Mapping SO₂ frost on Io by the modeling of NIMS hyperspectral images. *Icarus* 149, 107–132.

- Feaga, L. M., McGrath, M. A., Feldman, P. D., 2009. Io's dayside SO₂ atmosphere. *Icarus* 201, 570–584.
- Feldman, P. D., Strobel, D. F., Moos, H. W., Retherford, K., Wolven, B. C., McGrath, M. A., Roesler, F. L., Woodward, R. C., Oliverson, R. J., Ballester, G. E. 2000. Lyman- α imaging of the SO₂ distribution on Io, *Geophys. Res. Lett.* 27, 1787–1790.
- Formisano, V., 26 colleagues. 2003, Cassini-VIMS at Jupiter: Solar occultation measurements using Io, *Icarus* 166, 75–84.
- Frank, L. A., Paterson, W. R., Ackerson, K. L., Vasyliunas, V. M., Coroniti, F. V., Bolton, S. J., 1996. Plasma observations at Io with the Galileo spacecraft. *Science* 274, 394–395.
- Geissler, P. E., McEwen, A. S., Ip, W., Belton, M. J. S., Johnson, T. V., Smyth, W. H., Ingersoll, A. P. 1999. Galileo imaging of atmospheric emissions from Io. *Science* 285, 870–874.
- Geissler, P. E., McEwen, A. S., Porco, C., Strobel, D., Saur, J., Ajello, J., West, R. 2004. Cassini observations of Io's visible aurorae. *Icarus* 172, 127–140.
- Gratiy, S. L., Walker, A. C., Levin, D. A., Goldstein, D. B., Varghese, P. L., Trafton, L. M., Moore, C. H. 2010. Multi-wavelength simulations of atmospheric radiation from Io with a 3-D spherical-shell backward Monte Carlo radiative transfer model, *Icarus* 207, 394–408.
- Hapke, B., Wells, E., Wagner, J. 1981. Far-UV, visible, and near-IR reflectance spectra of frosts of H₂O, CO₂, NH₃, and SO₂. *Icarus*, 47, 361–367.
- Jessup, K.- L., Spencer, J. R., Ballester, G. E., Howell, R. R., Roesler, F., Vigel, M., Yelle, R. 2004. The atmospheric signature of Io's Prometheus plume and anti-jovian hemisphere: evidence for a sublimation atmosphere, *Icarus* 169, 197–215.
- Jessup, K.- L., Spencer, J. R., Yelle, R. 2007. Sulfur volcanism on Io. *Icarus* 192, 24–40.
- Jessup, K.- L., Spencer, J. R. 2012. Characterizing Io's Pele, Tvashtar and Pillan plumes: Lessons learned from Hubble. *Icarus* 218, 378–405.
- Karkoschka, E. 1998, Methane, ammonia, and temperature measurements of the Jovian planets and Titan from CCD-spectrophotometry. *Icarus* 133, 134–146.
- Lellouch, E. 1996. Io's atmosphere: Not yet understood. *Icarus* 124, 1–21.
- Lellouch, E. 2005. Io's atmosphere and surface-atmosphere interactions, *Space Science Reviews* 116, 211–224.
- Lopes-Gautier, R. 2000. Volcanism on Io, In: Sigurdsson, H. (Editor-in-chief), *Encyclopedia of Volcanoes*, p. 709.
- Lopes, R. M. C., Kamp, L. W., Smythe, W. D., Mouginiis-Mark, P., Kargel, J., Radebaugh,

J., Turtle, E. P., Perry, J., Williams, D. A., Carlson, R. W., Doute, S. 2004. Lava lakes on Io: Observations of Io's volcanic activity from Galileo NIMS during the 2001 fly-bys. *Icarus* 169, 140–174.

Lopes, R. M. C., Spencer, J. R. 2007. *Io after Galileo: A new view of Jupiter's volcanic moon*, Springer Praxis Books / Geophysical Sciences, Berlin.

McEwen, A. S., Keszthelyi, L., Spencer, J. R., Schubert, G., Matson, D. L., Lopes-Gautier, R., Klaasen, K. P., Johnson, T. V., Head, J. W., Geissler, P., Fagents, S., Davies, A. G., Carr, M. H., Breneman, H. H., Belton, M. J. S. 1998a. High-temperature silicate volcanism on Jupiter's moon Io. *Science* 5373, 87–90.

McEwen, A. S., Keszthelyi, L., Geissler, P., Simonelli, D. P., Carr, M. H., Johnson, T. V., Klaasen, K. P., Breneman, H. H., Jones, T. J., Kaufman, J. M., Magee, K. P., Senske, D. A., Belton, M. J. S., Schubert, G. 1998b. Active volcanism on Io as seen by Galileo SSI, *Icarus* 135, 181–219.

McGrath, M. A., Belton, M. S., Spencer, J. R., Sartoretti, P. 2000. Spatially resolved spectroscopy of Io's Pele plume and SO₂ atmosphere. *Icarus* 146, 476–493.

McGrath, M. A., Lellouch, E., Strobel, D. F., Feldman, P. D., Johnson, R. E. 2004. Satellite atmospheres. In: Bagenal, F., Dowling, T. E., McKinnon, W. B. (Eds.) *Jupiter. The Planet, Satellites and Magnetosphere*. Cambridge planetary science, Vol. 1. Cambridge University Press, Cambridge, pp. 457–483.

Manatt, S. L., Lane, A. L. 1993. A compilation of the absorption cross-sections of SO₂ from 106 to 403 nm. *JQSRT* 50, 267–276.

Marchis, F., Le Mignant, D., Chaffee, F. H., Davies, A. G., Kwok, S. H., Prange, R., de Pater, I., Amico, P., Campbell, R., Fusco, T., Goodrich, R. W., Conrad, A. 2005. Keck AO survey of Io global volcanic activity between 2 and 5 μm . *Icarus* 176, 96–122.

Moore, C. H., Goldstein, D. B., Varghese, P. L., Trafton, L. M., Stewart, B. 2009. 1-D DSMC simulation of Io's atmospheric collapse and reformation during and after eclipse. *Icarus* 201, 585–597.

Moore, C.H., Miki, K., Goldstein, D.B., Varghese, P.L., Trafton, L.M., Stapelfeldt, K., Evans, R.W., 2010a. Modeling of Io's [O I] 6300 Å and [S II] 6716 Å auroral emission in eclipse. *Icarus* 207, 810–833.

Moore, C.H., Goldstein, D.B., Varghese, P.L., and Trafton, L.M. 2010b. Io's UV-V eclipse emission: Implications for Pele-type plumes. *Lunar Planet. Sci.* XXXXI, 2353 (abstract).

Oliveresen, R.J., Scherb, F., Smyth, W. H., Freed, M. E., Woodward, R. C. Jr, Marconi, M. L., Retherford, K. D., Lupie, O. L., Morgenthaler, J. P. 2001. Sunlit Io atmospheric [O I] 6300 Å emission and the plasma torus. *J. Geophys. Res.* 106, 26,183–26,193.

Pearce, R. W. B. and Gaydon, A. G. 1976. *The identification of molecular spectra*. 4th ed. Wiley, New York.

Rathbun, J. A., Spencer, J. R., Tamppari, L. K., Martin, T. Z., Barnard, L., Travis, L. D. 2003. Mapping of Io's thermal radiation by the Galileo photopolarimeter-radiometer (PPR) instrument. *Icarus* 169, 127–139.

Retherford, K. D., Moos, H. W., Strobel, D. F., Wolven, B. C. 2000. Io's equatorial spots: Morphology of neutral UV emissions. *J. Geophys. Res.* 105, A12, 21,157–27,165.

Retherford, K. D., Feldman, P. D., Moos, H. W., Strobel, D. F., Wolven, B. C., Oliveresen, R. J., McGrath, M. A., Roesler, F. L., Scherb, F., Ballester, G. E., Smyth, W. H., Bagenal, F. 2000. Io's UV aurora: Detection of neutral hydrogen and neutral chlorine. *Bull. Amer. Astron. Soc.* 32, 1055.

Retherford, K. D., Moos, H. W., Strobel, D. F. 2003. Io's auroral limb glow: Hubble Space Telescope FUV observations, *J. Geophys. Res.* 108, A8, pp. SIA 7-1, CiteID 1333.

Retherford, K. D., 20 colleagues. 2007. Io's atmospheric response to eclipse: UV aurorae observations. *Science* 318, 237–240.

Saur, J., Neubauer, F. M., Strobel, D. F., Summers, M.E. 2002. Interpretation of Galileo's Io plasma and field observations: The J10, I24, I27 flybys, and close polar passes. *J. Geophys. Res.* 107 (A12), 1422.

Saur, J., Strobel, D. F. 2004. Relative contributions of sublimation and volcanoes to Io's atmosphere inferred from its plasma interaction during solar eclipse. *Icarus* 171, 411–420.

Schneider, N.M. and Bagenal, F., 2006. Io's neutral clouds, plasma torus, and magnetospheric interaction. In: *Io after Galileo* (R. Lopes and J. Spencer, Eds.). Springer, Chichester, UK, pp. 265–286.

Schneider, N.M. and Trauger, J.T., 1995. The structure of the Io torus. *Astrophys. J.* 450, 450–462.

Sittler, E.C., and D.F. Strobel 1987. Io plasma torus electrons Voyager 1. *J. Geophys. Res.* 92, 5741-5762.

Spencer, J. R., & Schneider, N. M. 1996. Io on the eve of the Galileo mission, *Ann. Rev. Earth Planet Sci.* 24, 125–190.

Spencer, J. R., Sartoretti, P., Ballester, G. E., McEwen, A. S., Clarke, J. T., McGrath, M. A. 1997. Pele plume (Io): Observations with the Hubble Space Telescope. *Geophysical Res. Lett.* 24, 2471-2474.

Spencer, J.R., Jessup, K.L., McGrath, M.A., Ballester, G.E., Yelle, R. 2000. Discovery of gaseous S₂ in Io's Pele plume. *Science* 288, 1208–1210.

Spencer, J. R., Lellouch, E., Richter, M. J., Lopez-Valverde, M. A., Jessup, K. L., Greathouse, T. K., Flaud, J.-M. 2005. Mid-infrared detection of large longitudinal asymmetries in Io's SO₂ atmosphere. *Icarus* 176, 283–304.

Tsang, C. C. C., Spencer, J. R., Lellouch, E., Lopez-Valverde, M. A., Richter, M. J., Greathouse, T. K. 2012. Io's atmosphere: Constraints on sublimation support from density variations on seasonal timescales using NASA IRTF/TEXES observations from 2001 to 2010. *Icarus* 217, 277–296.

Trafton, L. M., Caldwell, J. J., Barnet, C., Cunningham, C. C. 1996. The gaseous sulfur dioxide abundance over Io's leading and trailing hemispheres: HST spectra of Io's $C^1B_2 - X^1A_1$ band of SO₂ near 2100 Å. *Astrophys. J.* 456, 384–392.

Walker, A. C., Gratiy, S. L., Goldstein, D. B., Moore, C. H., Varghese, P. L., Trafton, L. M., Levin, D. A., Stewart, B. 2010. A comprehensive numerical simulation of Io's sublimation-driven atmosphere, *Icarus* 207, 409–432.

Wamsteker, W. 1972. Narrow-band photometry of the Galilean satellites, *Communications of the Lunar and Planetary Laboratory* 9, 171–177.

Wong, M. C., Smyth, W. H. 2000. Model calculations for Io's atmosphere at eastern and western elongation. *Icarus* 146, 60–74.

Zhang, J., Goldstein, D., Varghese, P., Gimelshein, N., Gimelshein S., Levin, D., Trafton L. 2003a. DSMC Modeling of gasdynamics, radiation and fine particulates in Ionian volcanic jets. In: Ketsdever, A., Muntz, E. P. (Eds.), *Proc. 23rd International Symposium on Rarefied Gas Dynamics* 663. AIP, New York, 704-711.

Zhang, J., Goldstein, D. B., Varghese, P. L., Gimelshein, N. E., Gimelshein, S. F., Levin, D. A. 2003b. Simulation of gas dynamics and radiation in volcanic plumes on Io. *Icarus* 163, 182–197.

Zhang, J., Goldstein, D. B., Varghese, P. L., Trafton, L. M., Moore, C., Miki, K. 2004. Numerical modeling of Ionian volcanic plumes with entrained particulates. *Icarus* 172, 479–502.

Zolotov, M. Y, & Fegley, B. Jr. 2000. Eruption conditions of Pele volcano on chemistry of its volcanic plume. *Geophys. Res. Lett.* 27, 2789–2792,

ACCEPTED MANUSCRIPT

Highlights

Io's MUV aurorae have been observed and simulated in eclipse

Emission from SO₂, SO, and SI has been detected and simulated

The emission is consistent with dissociative excitation of SO₂ by torus electrons

The emission is brighter in the general wake region

A spectrum from an unidentified species was discovered

As much as a 5% non-thermal component to the torus electrons is implied